https://doi.org/10.5194/egusphere-2026-1905
Preprint. Discussion started: 11 May 2026

ODEM v1.0: an offline dust emission model for reanalysis-driven source estimation

Metin Baykara[1]

[1]Climate and Marine Sciences Department, Eurasia Institute of Earth Sciences, Istanbul Technical University, Maslak, Istanbul, 34469, Turkey

Correspondence: Metin Baykara (baykara@itu.edu.tr)

Abstract. Global dust emission estimates remain uncertain by a factor of two to three across models, with uncertainty arising from both the emission physics and the choice of meteorological forcing. Disentangling these two sources of uncertainty requires running the same emission scheme with different meteorological inputs, which is not possible in online models where the emission physics and the forcing are coupled within a single atmospheric model.

This paper presents ODEM v1.0 (Offline Dust Emission Model), a standalone Python implementation of the brittle fragmentation dust emission parameterization of Kok et al. (2014), following the implementation of Leung et al. (2023). ODEM accepts either ERA5 or MERRA-2 as meteorological forcing and produces gridded dust emission flux fields at the native spatiotemporal resolution of each reanalysis (0.25°, 1-hourly for ERA5; 0.5° × 0.625°, 1-hourly for MERRA-2). The model applies process-based emission physics – including soil particle size, moisture inhibition, aerodynamic drag partition, and turbulent intermittency corrections – to every land grid cell independently in a single forward pass with no spin-up requirement.

For the year 2006, ODEM driven by ERA5 at 1-hourly resolution produces a global PM20 emission of 15 539 Tg yr^{-1} and ODEM driven by MERRA-2 produces 12 747 Tg yr^{-1}. These values exceed the observationally constrained PM20 budget of 5000 ± 1600 Tg yr^{-1} by factors of 3.1 and 2.5, respectively. This overshoot is a known property of the Kok et al. (2014) emission equation at its default calibration: Leung et al. (2023) report a comparable factor of 2.3 for their unnormalised scheme using the same equation, indicating that current emission physics cannot constrain the absolute magnitude from first principles. ERA5 produces 22 % more emission than MERRA-2, consistent with known differences in reanalysis friction velocity fields, particularly over North Africa. A sensitivity experiment using ERA5 at 3-hourly resolution yields 15 521 Tg yr^{-1} (0.1 % lower), confirming that the turbulent intermittency correction effectively accounts for sub-timestep wind variability. Both experiments produce roughly an order of magnitude higher emission than the MERRA-2 online GOCART scheme (1564 Tg yr^{-1}), consistent with the known underestimation by empirical schemes relative to observational constraints.

1 Introduction

Mineral dust is the largest contributor to global aerosol optical depth and the most abundant tropospheric aerosol by mass, with emission fluxes estimated at 5000 ± 1600 Tg yr^{-1} for particles up to 20 μm in diameter (PM20) (Kok et al., 2021). Through direct scattering and absorption of solar and terrestrial radiation, indirect effects on cloud microphysics, and fertilisation of

https://doi.org/10.5194/egusphere-2026-1905
Preprint. Discussion started: 11 May 2026

remote marine and terrestrial ecosystems, dust affects the Earth system at scales ranging from local air quality to global radiative forcing (Mahowald et al., 2006; Tegen and Fung, 1994). Despite its importance, global dust emission remains difficult to constrain: multi-model intercomparisons show that simulated emission budgets differ by a factor of two to three (Huneeus et al., 2011; Kok et al., 2021).

The primary control on dust emission is the surface friction velocity u_*, which must exceed a threshold determined by soil particle size, surface moisture, and the drag exerted by roughness elements. Early formulations linked dust emission to surface wind through the saltation bombardment mechanism (Marticorena and Bergametti, 1995), with threshold friction velocity depending on soil texture and surface properties (Shao and Lu, 2000). Alternative size-resolved schemes have since been proposed (Shao, 2004), but the representation of the emitted size distribution remained a key uncertainty. The brittle fragmentation theory of Kok (2011) provides a physically grounded framework for the dust emission size distribution, and Kok et al. (2014) built on this to develop an improved emission parameterization in which the vertical dust flux scales with excess of u_* above threshold through a fragmentation-dependent exponent. Leung et al. (2023) implemented the Kok et al. (2014) scheme in the Community Earth System Model and demonstrated that a process-based formulation, constrained by observations, substantially reduces the spread in simulated global budgets relative to empirical schemes.

Existing dust emission schemes are embedded in online atmospheric models, where the emission physics and the meteorological forcing are produced by the same model. Since both the meteorology and the physics differ across models, differences in simulated emission cannot be attributed to either factor alone. While some regional models can be driven by prescribed meteorology (e.g. CHIMERE, Menut et al., 2013; DREAM, Nickovic et al., 2001), and global schemes such as GOCART (Ginoux et al., 2001), DEAD (Zender et al., 2003), and the AFWA scheme (LeGrand et al., 2023) have been widely used in offline or semi-offline configurations, these employ empirical emission formulations rather than the process-based parameterization of Kok et al. (2014). No standalone global implementation of the Kok et al. (2014) scheme exists that accepts arbitrary reanalysis forcing. An offline model that reads externally prescribed reanalysis fields and applies the emission physics to them separates these two sources of uncertainty: running the same scheme with different reanalyses quantifies the sensitivity of emission to meteorological forcing with the physics held constant.

ODEM (Offline Dust Emission Model) is a standalone Python implementation of the Kok et al. (2014) dust emission parameterization, following the parameter choices and implementation of Leung et al. (2023). The emission physics are deliberately kept identical to Leung et al. (2023) so that differences between experiments can be attributed to the meteorological forcing alone — a comparison that is not possible within a coupled model such as CESM, where the atmospheric and land surface models generate the forcing fields internally and cannot be replaced independently. It accepts either ERA5 (Hersbach et al., 2020) or MERRA-2 (Gelaro et al., 2017) as meteorological forcing, and produces gridded dust emission flux fields at the native reanalysis resolution. The output fields are intended to serve as direct input to Lagrangian trajectory models such as FLEXPART (Pisso et al., 2019) and HYSPLIT (Stein et al., 2015), where gridded emission can be combined with source-receptor relationships to attribute dust loading along individual transport pathways. More broadly, ODEM is intended for research groups that need consistent, reproducible dust emission fields for source attribution, air quality assessment, or climate model evaluation without running a full atmospheric model. An emission processing framework that ingests ODEM output, extracts

https://doi.org/10.5194/egusphere-2026-1905
Preprint. Discussion started: 11 May 2026

trajectory-level dust flux, and converts mass emission to particulate number concentrations for air quality applications is currently under development and will be described in a companion paper. ODEM operates with a single forward pass per timestep using NumPy-vectorised operations on global two-dimensional arrays; it requires no spin-up period and has no inter-timestep memory.

This paper describes ODEM v1.0. Sect. 2 details the emission physics, static input datasets, and numerical implementation. Sect. 3 describes the ERA5 and MERRA-2 simulation experiments and the evaluation datasets. Sect. 4 presents results for the year 2006 and evaluates the simulated dust budget against independent observational constraints. Sect. 5 discusses forcing sensitivity and model limitations. Conclusions are given in Sect. 6.

2 Model description

2.1 Overview and workflow

ODEM (Offline Dust Emission Model) is a process-based, globally applicable dust emission model that accepts any gridded reanalysis product as meteorological forcing. The model operates in a single forward pass: for each timestep in the forcing dataset, ODEM reads the required meteorological fields, applies the emission physics to every grid cell independently, and writes the resulting dust emission flux to a NetCDF output file. There is no spin-up period and no coupling between timesteps; each timestep is self-contained.

The model workflow is illustrated in Fig. 1. Static input datasets (land cover, soil properties, aerodynamic roughness, and leaf area index) are preprocessed once and regridded to the forcing resolution. At runtime, ODEM reads these static fields together with the time-varying meteorological forcing and computes the emission flux at each timestep. The output spatial resolution inherits from the forcing: 0.25° for ERA5 and 0.5°×0.625° for MERRA-2. Temporal resolution likewise matches the forcing (1-hourly for both ERA5 and MERRA-2 in the experiments presented here).

https://doi.org/10.5194/egusphere-2026-1905
Preprint. Discussion started: 11 May 2026

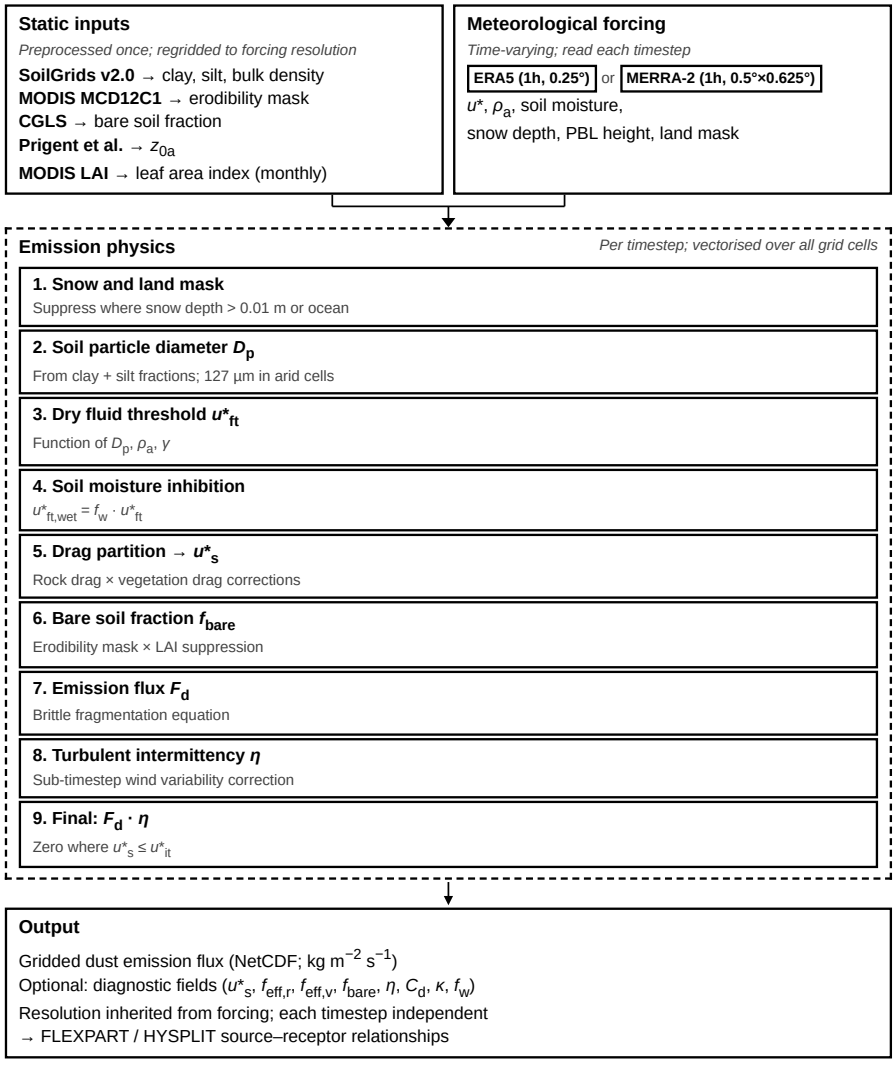

Figure 1. Schematic workflow of ODEM v1.0. Static datasets (left) and time-varying meteorological forcing (top) are combined to compute gridded dust emission fluxes. The output emission fields can be ingested by downstream applications such as Lagrangian trajectory models.

2.2 Static input datasets

Table 1 lists all static input datasets used by ODEM. These fields are time-invariant or updated at monthly timescales (leaf area index) and are preprocessed to the target model grid prior to a model run.

https://doi.org/10.5194/egusphere-2026-1905
Preprint. Discussion started: 11 May 2026

Table 1. Static input datasets used by ODEM v1.0. All datasets are freely available at the cited sources.

Dataset	Variable	Native resolution	Reference
SoilGrids v2.0	Clay fraction, silt fraction, bulk density	250 m	Poggio et al. (2021)
MODIS MCD12C1	Land cover, erodibility mask	0.05°	Friedl and Sulla-Menashe (2015)
CGLS	Bare soil fraction	300 m	Copernicus Global Land Service (2020)
Prigent et al.	Aerodynamic roughness z_{0a}	0.25°	Prigent et al. (2005)
MODIS LAI	Leaf area index (monthly)	0.25°	Myneni et al. (2015)

Soil clay and silt fractions from SoilGrids v2.0 are used to derive the median soil particle diameter (Sect. 2.4.2) and the soil moisture inhibition threshold (Sect. 2.4.4). The MODIS land cover product (MCD12C1, IGBP classification) is used to construct the erodibility mask: grid cells classified as barren, open shrubland, or sparse vegetation are assigned positive erodibility fractions; forests, water bodies, permanent snow, and urban areas are masked as non-erodible. The CGLS bare soil fraction further modulates emission within erodible cells. Aerodynamic roughness length z_{0a} from Prigent et al. (2005) is derived from satellite radar backscatter and represents the aeolian (wind-facing) roughness at 0.25° resolution. Monthly MODIS leaf area index (LAI) is used in both the vegetation drag partition (Sect. 2.4.5) and the bare soil fraction calculation.

Figure 2 shows four of these fields at the ERA5 grid resolution. The erodibility fraction (panel a) highlights the Sahara, Arabian Peninsula, and central Asian deserts as the dominant source regions, with secondary sources in Patagonia, southern Africa, and Australia. Topsoil clay fraction (panel b) controls the emission threshold and the size distribution of emitted particles; the lowest clay fractions coincide with sandy desert interiors. Aerodynamic roughness z_{0a} (panel c) modulates the drag partition: low values in the central Sahara indicate smooth surfaces where a large fraction of the wind shear acts directly on the erodible soil. Annual mean LAI (panel d) shows that vegetation cover suppresses emission across the Sahel, semi-arid Asia, and the Australian margins.

https://doi.org/10.5194/egusphere-2026-1905
Preprint. Discussion started: 11 May 2026

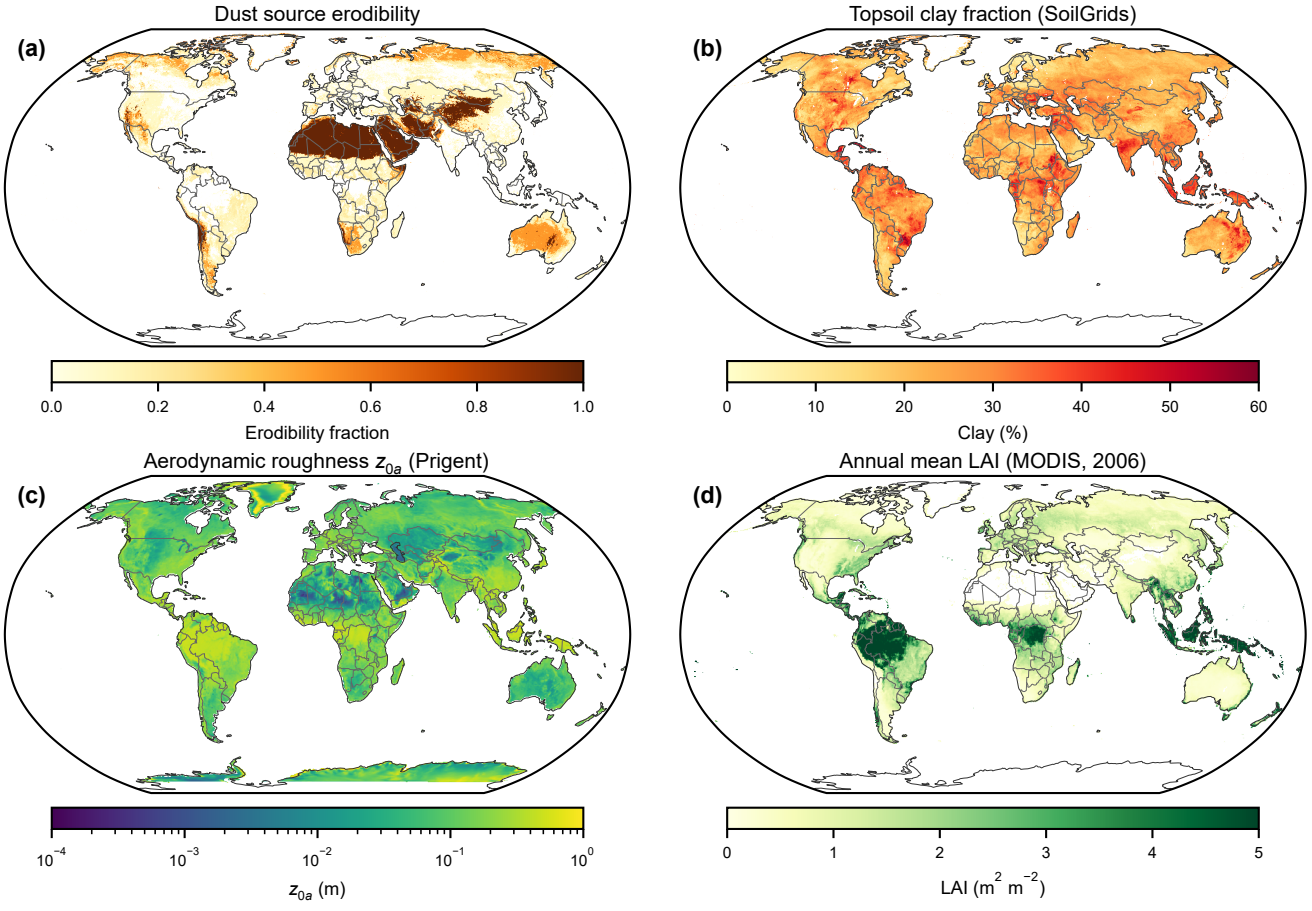

Figure 2. Static input fields used by ODEM, shown at 0.25° resolution: (a) dust source erodibility fraction derived from MODIS land cover, (b) topsoil clay fraction from SoilGrids v2.0, (c) aerodynamic roughness length z_{0a} from Prigent et al. (2005), and (d) annual mean leaf area index from MODIS (2006).

2.3 Meteorological forcing

ODEM accepts either ERA5 (Hersbach et al., 2020) or MERRA-2 (Gelaro et al., 2017) as meteorological forcing. Table 2 lists the variable mapping between the two reanalyses. The key meteorological input is the surface friction velocity u_*, which drives dust emission nonlinearly. For ERA5, u_* is taken directly from the forecast field `zust`. For MERRA-2, the equivalent variable is `USTAR` from the `M2T1NXFLX` collection. Air density is computed from 2-metre temperature, dewpoint temperature, and surface pressure for ERA5 (via the Magnus formula); for MERRA-2 it is provided directly as `RHOA`.

https://doi.org/10.5194/egusphere-2026-1905
Preprint. Discussion started: 11 May 2026

Table 2. Mapping of ODEM internal variables to ERA5 and MERRA-2 fields. MERRA-2 collection codes: `FLX` = M2T1NXFLX; `LND` = M2T1NXLND. For ERA5, air density is derived from `t2m`, `d2m`, and `sp` via the Magnus formula.

Variable	ERA5	MERRA-2	Coll.
Friction vel. u_*	`zust`	`USTAR`	FLX
Air density ρ_a	derived	`RHOA`	FLX
Soil moisture	`swvl1`	`SFMC`	LND
Snow depth	`sd`	`SNODP`	LND
PBL height	`blh`	`PBLH`	FLX
Land mask	`lsm`	`DISPH`>0	FLX

2.4 Emission physics

ODEM implements the dust emission parameterization of Kok et al. (2014), based on the brittle fragmentation theory of Kok (2011), with the implementation choices and parameter values of Leung et al. (2023). The following subsections describe each component in order of application.

2.4.1 Snow and land masking

Dust emission is suppressed at any grid cell where snow depth exceeds 0.01 m, following the approach of Leung et al. (2023). Emission is further restricted to land grid cells as determined by the land–sea mask of the respective reanalysis product.

2.4.2 Median soil particle diameter

The median soil particle diameter D_p is estimated from soil texture following Leung et al. (2023). In arid regions (LAI $<$ $1\,\mathrm{m^2\,m^{-2}}$), a fixed value of $D_p = 127\,\mu$m is used. In non-arid regions, D_p is estimated from the fine soil fraction:

$$D_p = \Psi_0 + \Psi_1(f_{\mathrm{silt}} + f_{\mathrm{clay}}), \tag{1}$$

where f_{silt} and f_{clay} are the silt and clay mass fractions (%) from SoilGrids v2.0, $\Psi_0 = 7.8\times10^{-6}$ m, and $\Psi_1 = 1.24\times10^{-4}$ m are regression coefficients from Leung et al. (2023). The surface roughness length z_{0s} (smooth surface) is derived from D_p as $z_{0s} = 2\,D_p/30$ (Leung et al., 2023), a factor-of-two increase over the classical Nikuradse relation ($D_p/30$) that accounts for the greater effective roughness of natural soil surfaces compared to uniform sand grains.

2.4.3 Fluid threshold friction velocity

The dry fluid threshold friction velocity $u^0_{*\mathrm{ft}}$ is computed following Shao and Lu (2000):

$$u^0_{*\mathrm{ft}}(D_p) = \sqrt{\frac{A_{\mathrm{SL}}}{\rho_a}\left(\rho_p g D_p + \frac{\gamma}{D_p}\right)}, \tag{2}$$

https://doi.org/10.5194/egusphere-2026-1905
Preprint. Discussion started: 11 May 2026

where $\rho_p = 2650\,\mathrm{kg\,m^{-3}}$ is the particle density, g is gravitational acceleration, $\gamma = 1.65 \times 10^{-4}\,\mathrm{kg\,s^{-2}}$ is the interparticle cohesion parameter, and $A_{\mathrm{SL}} = 0.0123$ is the aerodynamic force coefficient (Shao and Lu, 2000). The impact threshold $u_{*\mathrm{it}} = B_{\mathrm{it}} \cdot u^0_{*\mathrm{ft}}$, where $B_{\mathrm{it}} = 0.82$ (Kok, 2011), is used as the operative emission threshold.

2.4.4 Soil moisture inhibition

Surface soil moisture increases the threshold friction velocity through capillary and adhesion forces. Following Fécan et al. (1999):

$$f_w = \begin{cases} \sqrt{1 + 1.21\,(w - w')^{0.68}} & \text{if } w > w' \\ 1 & \text{otherwise,} \end{cases} \tag{3}$$

where w is gravimetric water content (%) and w' is the clay-dependent threshold:

$$w' = 0.17\,f_{\mathrm{clay}} + 0.0014\,f^2_{\mathrm{clay}}, \tag{4}$$

with f_{clay} in percent. The wet fluid threshold is then $u^{\mathrm{wet}}_{*\mathrm{ft}} = f_w \cdot u^0_{*\mathrm{ft}}$. Volumetric soil moisture from the forcing (ERA5 `swvl1`, MERRA-2 `SFMC`) is converted to gravimetric water content using bulk density from SoilGrids v2.0.

2.4.5 Rock drag partition

The surface friction velocity u_{*s} — the fraction of total wind shear acting on erodible soil — is lower than u_* due to momentum absorption by non-erodible roughness elements (rocks, vegetation). ODEM combines the two contributions multiplicatively:

$$u_{*s} = u_* \cdot f_{\mathrm{eff,r}} \cdot f_{\mathrm{eff,v}}, \tag{5}$$

where $f_{\mathrm{eff,r}}$ and $f_{\mathrm{eff,v}}$ are the rock and vegetation efficiency factors. Following Marticorena and Bergametti (1995), the rock drag partition efficiency is:

$$f_{\mathrm{eff,r}} = 1 - \frac{\ln(z_{0a}/z_{0s})}{\ln\left(0.7\,(X/z_{0s})^{0.8}\right)}, \tag{6}$$

where z_{0a} is the aeolian aerodynamic roughness length from Prigent et al. (2005), $z_{0s} = 2\,D_p/30$ is the smooth surface roughness, and $X = 10.0\,\mathrm{m}$ is the inter-obstacle distance (Marticorena and Bergametti, 1995). Values are clipped to $[0.001, 1]$.

2.4.6 Vegetation drag partition

Following Okin (2008), the vegetation efficiency factor is:

https://doi.org/10.5194/egusphere-2026-1905
Preprint. Discussion started: 11 May 2026

$$f_{\text{eff,v}} = f_0 + (1 - f_0)\frac{K}{K + c}, \tag{7}$$

where $K = \pi/(2\,\text{VAI})$ is a gap-size parameter (VAI $\approx$ LAI), $c = 4.8$ is the ratio of e-folding distance to vegetation height (Okin, 2008), and $f_0 = 0.32$ is the friction velocity ratio immediately behind the obstacle (Okin, 2008; Leung et al., 2023). For bare surfaces (LAI $= 0$), $K \to \infty$ and $f_{\text{eff,v}} = 1$; in the implementation a floor of VAI $= 10^{-6}$ is applied to avoid numerical overflow.

2.4.7 Bare soil fraction

The bare soil fraction f_{bare} modulates the total emission per grid cell by accounting for the fraction of land surface that is both erodible and free of vegetation:

$$f_{\text{bare}} = f_{\text{erod}} \cdot \max\left(0, 1 - \frac{\text{LAI}}{\text{LAI}_{\text{thr}}}\right), \tag{8}$$

where f_{erod} is the MODIS-derived erodibility fraction and $\text{LAI}_{\text{thr}} = 1.0\,\text{m}^2\,\text{m}^{-2}$ is the LAI above which emission is fully suppressed within an erodible cell (Leung et al., 2023).

2.4.8 Emission flux

The dust emission flux is computed following Kok et al. (2014):

$$F_d = C_{\text{tune}} \cdot C_d \cdot f_{\text{bare}} \cdot f_{\text{clay}} \cdot \rho_a \cdot \frac{u_{*s}^2 - u_{*\text{it}}^2}{u_{*\text{it}}} \cdot \left(\frac{u_{*s}}{u_{*\text{it}}}\right)^{\kappa} \cdot \eta, \tag{9}$$

valid only where $u_{*s} > u_{*\text{it}}$; otherwise $F_d = 0$.

The terms in Eq. (9) are:

- $C_{\text{tune}} = 0.05$ — global tuning constant calibrated by Leung et al. (2023) against MERRA-2 dust emission.
- C_d — soil erodibility coefficient (Kok et al., 2014):

  $$C_d = C_{d0} \exp\left[-C_e \frac{u_{*\text{st}} - u_{*\text{st}}^0}{u_{*\text{st}}^0}\right],$$

  where $C_{d0} = 4.4 \times 10^{-5}$ and $C_e = 2.0$. The standardised fluid threshold $u_{*\text{st}} = u_{*\text{ft}}^{\text{wet}} \sqrt{\rho_a/\rho_{a0}}$ accounts for air density variations, with reference density $\rho_{a0} = 1.225\,\text{kg}\,\text{m}^{-3}$.
- $f'_{\text{clay}} = \min(f_{\text{clay}}/100,\, 0.20)$ — clay mass fraction as a dimensionless ratio (capped at 0.20). Note that f_{clay} in Eqs. (4) and (1) is in percent (0–100), whereas f'_{clay} here is a fraction (0–1). This term scales emission through the effect of clay particles on the size distribution of saltating grains (Kok, 2011).

https://doi.org/10.5194/egusphere-2026-1905
Preprint. Discussion started: 11 May 2026

- $\kappa = C_\alpha(u_{*\mathrm{st}} - u^0_{*\mathrm{st}})/u^0_{*\mathrm{st}}$ — fragmentation exponent (capped at 3), with $C_\alpha = 2.7$ and $u^0_{*\mathrm{st}} = 0.16\,\mathrm{m\,s^{-1}}$ (Kok et al., 2014).
- η — intermittency correction (Sect. 2.4.9).

2.4.9 Turbulent intermittency

At coarse temporal resolution (hours), the mean friction velocity u_* may remain below the emission threshold even though sub-hourly turbulent gusts would intermittently exceed it. Following Comola et al. (2019), ODEM corrects for this by computing the fraction of time η within each timestep during which saltation is active.

Wind speed fluctuations at $z_{\mathrm{ref}} = 10\,\mathrm{m}$ are assumed to follow a Gaussian distribution with mean $\bar{u} = u_* \ln(z_{\mathrm{ref}}/z_0)/\kappa_{\mathrm{vK}}$ (where $\kappa_{\mathrm{vK}} = 0.4$ is the von Kármán constant) and standard deviation $\sigma_u \approx 2.3\,u_*$ (Panofsky et al., 1977). The threshold wind speeds u_{ft} and u_{it} at 10 m are obtained by inverting the log-law: $u_{\mathrm{ft}} = u_{*\mathrm{ft}} \ln(z_{\mathrm{ref}}/z_0)/\kappa_{\mathrm{vK}}$, and analogously for u_{it}. The intermittency factor is:

$$\eta = P(u > u_{\mathrm{ft}}) + \nu \cdot [P(u > u_{\mathrm{it}}) - P(u > u_{\mathrm{ft}})]\,, \tag{10}$$

where $P(u > u_{\mathrm{ft}})$ and $P(u > u_{\mathrm{it}})$ are the exceedance probabilities derived from the Gaussian CDF. The mean threshold crossing rate ν is the expected number of up-crossings of u_{it} per unit time, computed from the Rice formula (Eq. 5 in Comola et al., 2019): $\nu = \frac{1}{2\pi}\frac{\sigma_{\dot{u}}}{\sigma_u}\exp\left[-\frac{(u_{\mathrm{it}}-\bar{u})^2}{2\sigma_u^2}\right]$, where $\sigma_{\dot{u}} = 2\pi\sigma_u/T_L$ and T_L is the Lagrangian integral timescale estimated from the boundary layer height ($T_L = 0.3\,h_{\mathrm{BL}}/\sigma_u$). When boundary layer height is not available in the forcing, $\eta = 1$ (all time emitting when $u_{*s} > u_{*\mathrm{it}}$).

2.5 Numerical implementation

2.5.1 Code structure

ODEM is implemented in Python 3 as a single-file module (`odem.py`) with two main components: an `InputData` class that handles data loading and regridding, and a `compute_emission()` function that evaluates the emission physics. The model depends on NumPy, SciPy, xarray, and netCDF4. A companion verification script (`odem_verify.py`) tests the emission physics against 38 independently computed scenarios spanning the full parameter range; all pass within floating-point tolerance.

The `InputData` class provides a unified interface to both ERA5 and MERRA-2 forcing. Internally, the class dispatches to reanalysis-specific loading routines that map variable names to a common set of internal fields (Table 2). For ERA5, air density is computed from 2 m temperature, dewpoint, and surface pressure via the Magnus formula; for MERRA-2, air density is read directly from the `RHOA` field. The emission physics code is independent of the forcing source; only the `InputData` class changes between ERA5 and MERRA-2 runs.

https://doi.org/10.5194/egusphere-2026-1905
Preprint. Discussion started: 11 May 2026

2.5.2 Gridding and regridding

The model operates on the native grid of the chosen reanalysis: 721×1440 cells (lat $\times$ lon) for ERA5 at 0.25° resolution, or 361×576 cells for MERRA-2 at $0.5° \times 0.625°$ resolution. Static input datasets are regridded to the target grid at initialisation using nearest-neighbour interpolation via SciPy's `RegularGridInterpolator`. Nearest-neighbour is chosen over bilinear interpolation to preserve the categorical nature of erodibility fractions and to avoid introducing spurious intermediate values in fields such as land cover class.

2.5.3 Time loop and memory management

All emission physics are evaluated as vectorized NumPy operations on full two-dimensional arrays; there are no per-cell loops. The main time loop iterates over individual timesteps (1-hourly for both ERA5 and MERRA-2 in this study, though any temporal resolution is supported). At each timestep, only the current meteorological fields and the pre-loaded static arrays are held in memory. Emission fluxes are written to monthly NetCDF files and accumulated into running sums for annual mean and maximum fields. Peak memory usage depends on the forcing grid: approximately 4 GB for MERRA-2 (208 k cells) and 16 GB for ERA5 (1.04 M cells).

For multi-file forcing (e.g. 12 monthly ERA5 files or 365 daily MERRA-2 files), the `InputData` class tracks file boundaries and opens files lazily as the time index advances. Monthly output files are finalised and closed at each month boundary.

2.5.4 Output format

ODEM produces three types of output, all in NetCDF4 format with zlib compression (level 4):

1. **Monthly emission files** (`odem_YYYYMM.nc`): dust emission flux F_d ($\mathrm{kg\,m^{-2}\,s^{-1}}$) at each timestep, stored as a three-dimensional array (time $\times$ lat $\times$ lon).

2. **Annual summary** (`odem_annual.nc`): time-mean emission flux $\overline{F_d}$ and maximum instantaneous flux $F_{d,\mathrm{max}}$, both as two-dimensional arrays.

3. **Diagnostic fields** (`odem_diag_mean.nc`, optional): time-mean values of all intermediate variables, including u_{*s}, $u_{*\mathrm{it}}$, $f_{\mathrm{eff,r}}$, $f_{\mathrm{eff,v}}$, f_{bare}, η, C_d, κ, D_p, and the soil moisture inhibition factor f_w. These fields enable component-level verification and attribution of emission differences between experiments.

2.5.5 Command-line interface

The model is invoked from the command line with mutually exclusive flags `--era5` and `--merra2` specifying the forcing source, followed by paths to the required static datasets. The global tuning constant C_{tune} can be overridden via `--C-tune`. An optional `--save-diags` flag enables diagnostic output. A typical invocation processes one calendar month; full-year simulations are run as 12 sequential monthly jobs.

https://doi.org/10.5194/egusphere-2026-1905
Preprint. Discussion started: 11 May 2026

Table 3. Computational cost for a full-year (2006) ODEM simulation.

	ERA5	M2
Grid cells	1 038 240	207 936
Timesteps yr^{-1}	8760	8760
Wall time (per month)	∼4 h	∼22 min
Wall time (12 months, sequential)	∼48 h	∼4.5 h
Peak memory	16 GB	4 GB
Output size	∼3.5 GB	∼250 MB

2.5.6 Computational cost

Table 3 summarises the computational cost for a one-year global simulation. The dominant cost is I/O: reading forcing data and writing compressed NetCDF output. The emission physics evaluation itself accounts for less than 30 % of wall time. ODEM requires Python 3.10 or later with NumPy, SciPy, xarray, and netCDF4. Minimum hardware is a single CPU core and 4 GB RAM. Because each month is independent, the 12 monthly jobs can be run in parallel; the ERA5 benchmarks in Table 3 were obtained on CSC Puhti (Intel Xeon Gold 6230, 16 GB RAM per task), while the MERRA-2 benchmark was obtained on a desktop workstation (Intel Core i7-12700, 32 GB RAM).

3 Experiments and evaluation data

3.1 Experiment design

Two main experiments are performed to evaluate ODEM and to quantify the sensitivity of dust emission to the choice of meteorological forcing. Both experiments cover the full calendar year 2006, use identical static input datasets and emission physics, and differ only in their meteorological forcing:

- **ODEM-ERA5**: driven by ERA5 reanalysis at 0.25° resolution and 1-hourly temporal resolution (8760 timesteps per year).
- **ODEM-M2**: driven by MERRA-2 reanalysis at 0.5° × 0.625° resolution and 1-hourly temporal resolution (8760 timesteps per year).

A sensitivity experiment, **ODEM-ERA5 (3 h)**, uses ERA5 at 3-hourly resolution (2920 timesteps per year) to assess the effect of temporal resolution on the emission estimate (Sect. 5.2).

The year 2006 is selected because (i) it falls within the period common to both reanalyses at full temporal resolution, (ii) the MERRA-2 global dust AOD for 2006 is within 5 % of the 2003–2020 mean, indicating a year without anomalous global dust activity, and (iii) both ERA5 and MERRA-2 provide complete 1-hourly archives for this year. A multi-year analysis is planned for ODEM v2.0 and is outside the scope of this model description paper. The static datasets (Table 1) are regridded

https://doi.org/10.5194/egusphere-2026-1905
Preprint. Discussion started: 11 May 2026

Table 4. Evaluation datasets used in this study.

Dataset	Variable	Resolution	Reference
MERRA-2 DUEM	Online dust emission flux (5 bins)	$0.5^\circ \times 0.625^\circ$, hourly	Randles et al. (2017)
Kok et al. (2021)	Global and regional dust budget	—	Kok et al. (2021)
DustCOMM v1	Dust loading, dust AOD	$2.5^\circ \times 2.0^\circ$	Adebiyi et al. (2020)

to the respective forcing resolution prior to each experiment using nearest-neighbour interpolation for all fields (Sect. 2.5.2). The MODIS land cover used for the erodibility mask is the 2006 MCD12C1 product. Because ODEM operates on the native reanalysis grid, emission is computed for every land grid cell that contains erodible soil. At the coarser MERRA-2 resolution ($0.5^\circ \times 0.625^\circ$, approximately 55 km), coastal grid cells may straddle land and ocean; the resulting emission is physically correct for the land fraction of the cell but may appear to extend over water when plotted (see Fig. 3).

The calibration constant $C_{\text{tune}} = 0.05$ is retained from Leung et al. (2023) in both experiments. This value was originally calibrated against MERRA-2 online dust emission in the Community Earth System Model; its applicability to ERA5 forcing is evaluated in Sect. 5.

3.2 Evaluation datasets

Direct observational validation of dust emission flux is not possible because no global measurements of this quantity exist. Instead, the ODEM output is evaluated against (i) model-based emission estimates that assimilate aerosol observations, (ii) observationally constrained dust budgets, and (iii) satellite-derived dust loading fields. The evaluation datasets are summarised in Table 4.

3.2.1 MERRA-2 online dust emission (DUEM)

The MERRA-2 aerosol reanalysis employs the GOCART dust emission scheme online within the GEOS-5 atmospheric model and assimilates MODIS aerosol optical depth (AOD) observations to adjust aerosol fields (Randles et al., 2017). Dust emission flux is archived in the `M2T1NXADG` collection as the `DUEM` variable, summed across five particle size bins (0.1–6 μm effective radius). Although MERRA-2 DUEM is a model product rather than a direct observation, it provides a physically consistent, observation-constrained estimate of dust emission at high spatiotemporal resolution and serves as a reference for qualitative comparison of spatial and temporal emission patterns.

3.2.2 Observational budget constraints

Kok et al. (2021) combined satellite retrievals from MODIS, MISR, CALIOP, and IASI with AERONET ground-based measurements and dust deposition records to estimate the global dust emission budget. Their estimate of $5000 \pm 1600\,\text{Tg yr}^{-1}$ for particles with diameter $d < 20\,\mu$m (PM20) represents the most comprehensive observationally constrained budget to date.

https://doi.org/10.5194/egusphere-2026-1905
Preprint. Discussion started: 11 May 2026

ODEM inherits the Kok et al. (2014) emission equation with the global tuning constant $C_{\mathrm{tune}} = 0.05$ from Leung et al. (2023), who normalised their simulations to this PM20 constraint. Without such normalisation, ODEM is expected to overshoot the PM20 budget by a factor of $\sim$2.5 (see Sect. 4.1). Kok et al. (2021) also provide regional budget estimates for North Africa, the Middle East, and East Asia, which are used to evaluate the source apportionment produced by ODEM.

3.2.3 DustCOMM

DustCOMM (Dust Constraints from joint Observational-Modelling-experiMental analysis; Adebiyi et al., 2020) provides observationally constrained estimates of atmospheric dust loading and dust AOD at $2.5^\circ \times 2.0^\circ$ resolution, derived by combining six global model simulations (CESM, CNRM, GEOS-Chem, GISS, IMPACT, WRF-Chem) with satellite-derived dust AOD. The constrained dust loading fields include mean values and uncertainty estimates ($\pm 1\sigma$, $\pm 2\sigma$). Although DustCOMM characterises the atmospheric dust column rather than surface emission, the spatial pattern of dust loading provides an independent check on source region identification: regions of high loading should broadly coincide with regions of high emission and their immediate downwind areas.

3.3 Evaluation metrics

ODEM output is evaluated at three levels:

1. **Global budget**: annual total dust emission (Tg yr^{-1}) compared against the Kok et al. (2021) observational range.
2. **Regional budgets**: emission totals for major source regions (North Africa, Middle East, East Asia, and other regions) compared against Kok et al. (2021) regional estimates.
3. **Spatial patterns**: qualitative comparison of annual and seasonal emission maps with MERRA-2 DUEM, and spatial correlation of ODEM emission against DustCOMM dust loading as an independent check on source placement.

The ERA5 and MERRA-2 experiments are compared against each other to quantify the sensitivity of emission to meteorological forcing. Differences are discussed in the context of the friction velocity fields of the two reanalyses (Sect. 5.1).

4 Results

4.1 Global dust budget

Table 5 summarises the global annual dust emission totals for 2006. ODEM-ERA5 produces 15 539 Tg yr^{-1} and ODEM-M2 produces 12 747 Tg yr^{-1}, exceeding the observationally constrained PM20 budget of 5000 ± 1600 Tg yr^{-1} (Kok et al., 2021) by factors of 3.1 and 2.5, respectively. This overshoot is a known property of the Kok et al. (2014) emission equation at its default calibration: Leung et al. (2023) report a comparable factor-of-2.3 overshoot for their unnormalised scheme using the same equation and $C_{\mathrm{tune}} = 0.05$, and note that "there are currently no first principles that can derive the essential dust

https://doi.org/10.5194/egusphere-2026-1905
Preprint. Discussion started: 11 May 2026

Table 5. Global annual dust emission totals for 2006.

Source	Emission (Tg yr^{-1})
ODEM-ERA5 (1 h)	15 539
ODEM-ERA5 (3 h)	15 521
ODEM-M2	12 747
MERRA-2 DUEM	1564
Kok et al. (2021)	5000 (3400–6600)*

*PM20 emission (particles with diameter $< 20\,\mu$m) reported by Kok et al. (2021). The range represents $\pm 1\sigma$ uncertainty. ODEM inherits the Kok et al. (2014) emission equation with the global tuning constant $C_{\mathrm{tune}} = 0.05$ from Leung et al. (2023), who normalised their simulations to this PM20 constraint. Without such normalisation, ODEM produces 2–3$\times$ the PM20 target, consistent with the factor-of-2.3 overshoot reported by Leung et al. (2023) for their unnormalised scheme and reflecting the documented inability of current emission physics to constrain the absolute emission magnitude from first principles (Leung et al., 2023).

emission proportionality constants to constrain modelled emissions at a correct order of magnitude." The ODEM-M2 value of 12 747 Tg yr^{-1} is within 9 % of the Leung et al. unnormalised total of $\sim$11 700 Tg yr^{-1}, confirming that ODEM faithfully reproduces the Kok et al. (2014) physics.

ERA5 produces 22 % more emission than MERRA-2, showing that reanalysis choice alone accounts for a substantial fraction of the uncertainty in the simulated global dust budget. A sensitivity run using ERA5 at 3-hourly temporal resolution yields 15 521 Tg yr^{-1}, within 0.1 % of the 1-hourly result, confirming that the turbulent intermittency correction effectively accounts for sub-timestep wind variability at 3-hourly resolution (Sect. 5.2).

Both ODEM experiments produce substantially higher emission than the MERRA-2 online GOCART scheme (DUEM), which yields only 1564 Tg yr^{-1} — roughly an order of magnitude lower than the ODEM estimates. This difference is expected: the GOCART scheme in MERRA-2 is an empirical parameterisation that is known to underestimate global dust emission relative to observational constraints (Kok et al., 2021), whereas ODEM applies the physically based brittle fragmentation scheme of Kok (2011).

4.2 Spatial distribution of emission

Figure 3 shows the annual mean dust emission flux for all three datasets. Both ODEM experiments reproduce the expected global source geography: North Africa dominates, with a pronounced maximum over the Bodélé Depression and western Sahara, followed by the Arabian Peninsula, Central and East Asia, and secondary sources in Patagonia, southern Africa, and Australia. ODEM-ERA5 and ODEM-M2 agree on source placement but differ in magnitude, particularly over the central Sahara where ERA5 produces stronger emission (Fig. 4).

The MERRA-2 DUEM map shows broadly similar source regions but at much lower flux magnitudes and with notably weaker emission in East Asia and Australia compared to the ODEM experiments. This is consistent with the global budget dif-

https://doi.org/10.5194/egusphere-2026-1905
Preprint. Discussion started: 11 May 2026

ference and reflects the different emission physics: the empirical GOCART scheme lacks the brittle fragmentation enhancement that amplifies emission at high friction velocities.

320 For the grid-cell comparison, ERA5 output is regridded to the MERRA-2 grid using bilinear interpolation (SciPy `RegularGridInterpolator`). The emission ratio ODEM-ERA5 / ODEM-M2 (Figure 5) shows that ERA5 and MERRA-2 produce comparable emission at most source cells after regridding (median ratio 0.99). The 22 % ERA5 global excess therefore arises not from a systematic cell-by-cell bias but from a small number of high-flux grid cells — principally over the central and western Sahara and the Tibetan Plateau margins — where ERA5 friction velocities are substantially higher than MERRA-2.

https://doi.org/10.5194/egusphere-2026-1905
Preprint. Discussion started: 11 May 2026

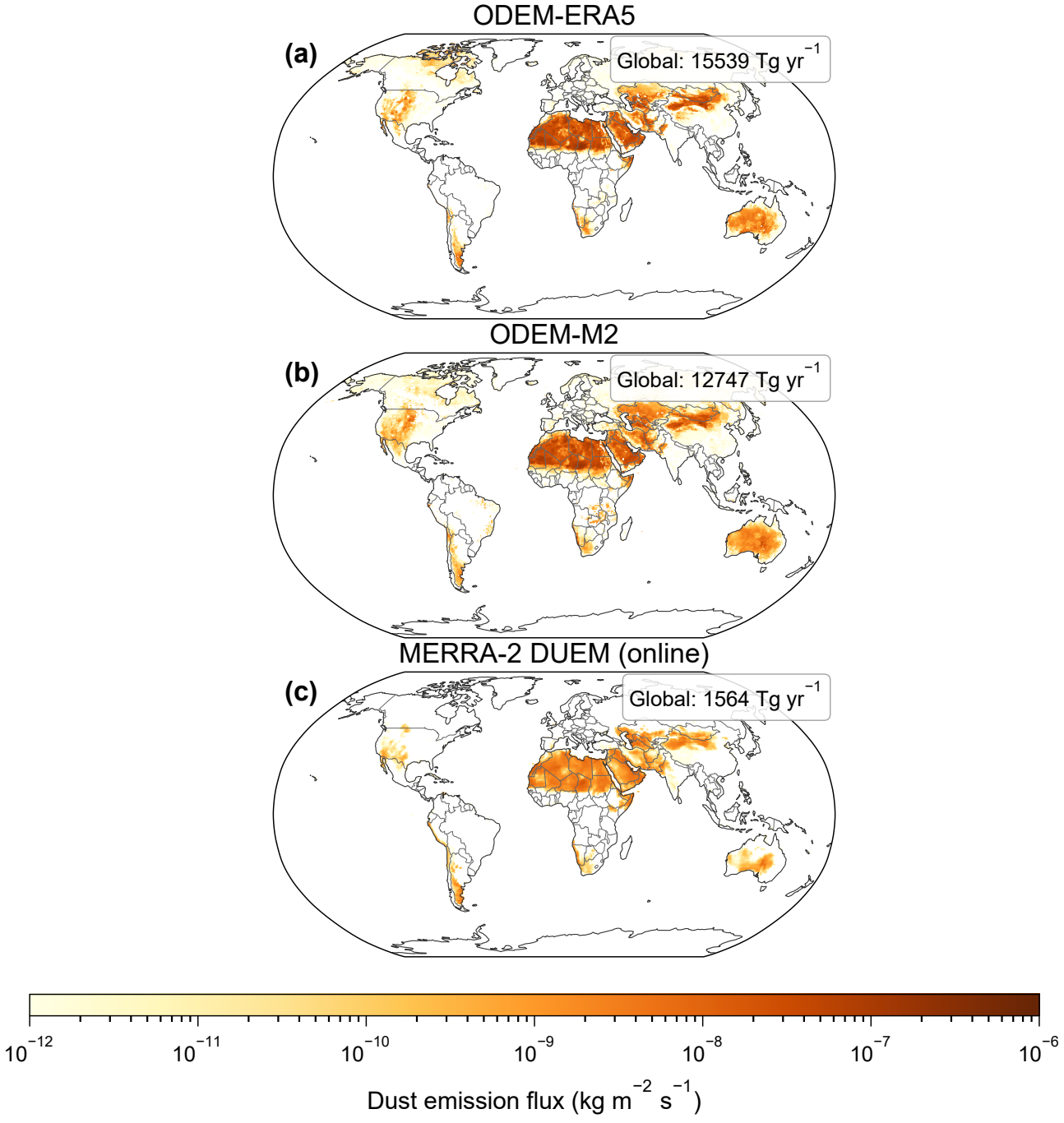

Figure 3. Annual mean dust emission flux (kg m^{-2} s^{-1}, log scale) for 2006: (a) ODEM-ERA5 at 0.25° resolution, (b) ODEM-M2 at 0.5° ×0.625° resolution, and (c) MERRA-2 DUEM online emission. Global annual totals are annotated in each panel.

https://doi.org/10.5194/egusphere-2026-1905
Preprint. Discussion started: 11 May 2026

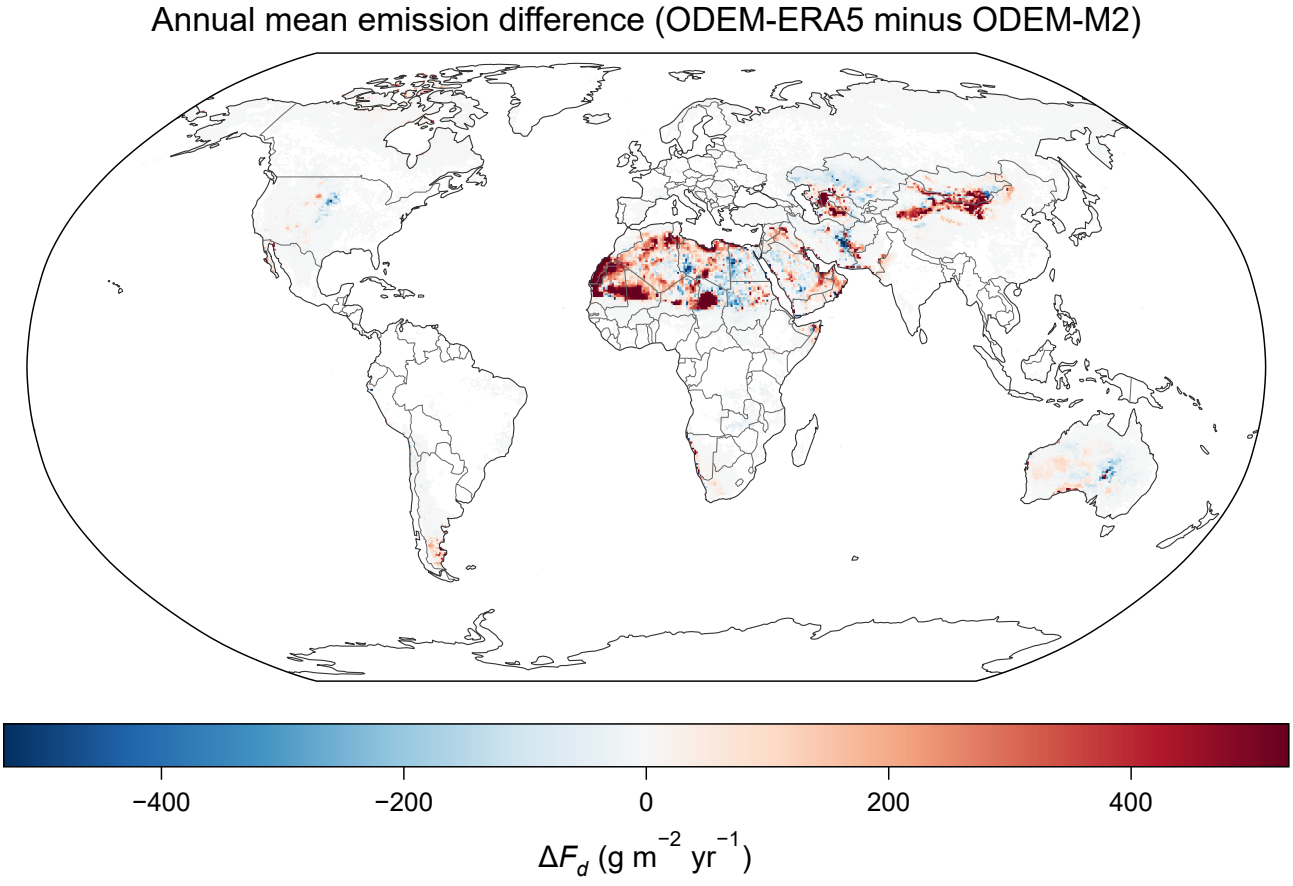

Figure 4. Difference in annual mean dust emission flux (ODEM-ERA5 minus ODEM-M2, g m^{-2} yr^{-1}) after regridding ERA5 output to the MERRA-2 grid. Red indicates higher emission in ERA5; blue indicates higher emission in MERRA-2.

https://doi.org/10.5194/egusphere-2026-1905
Preprint. Discussion started: 11 May 2026

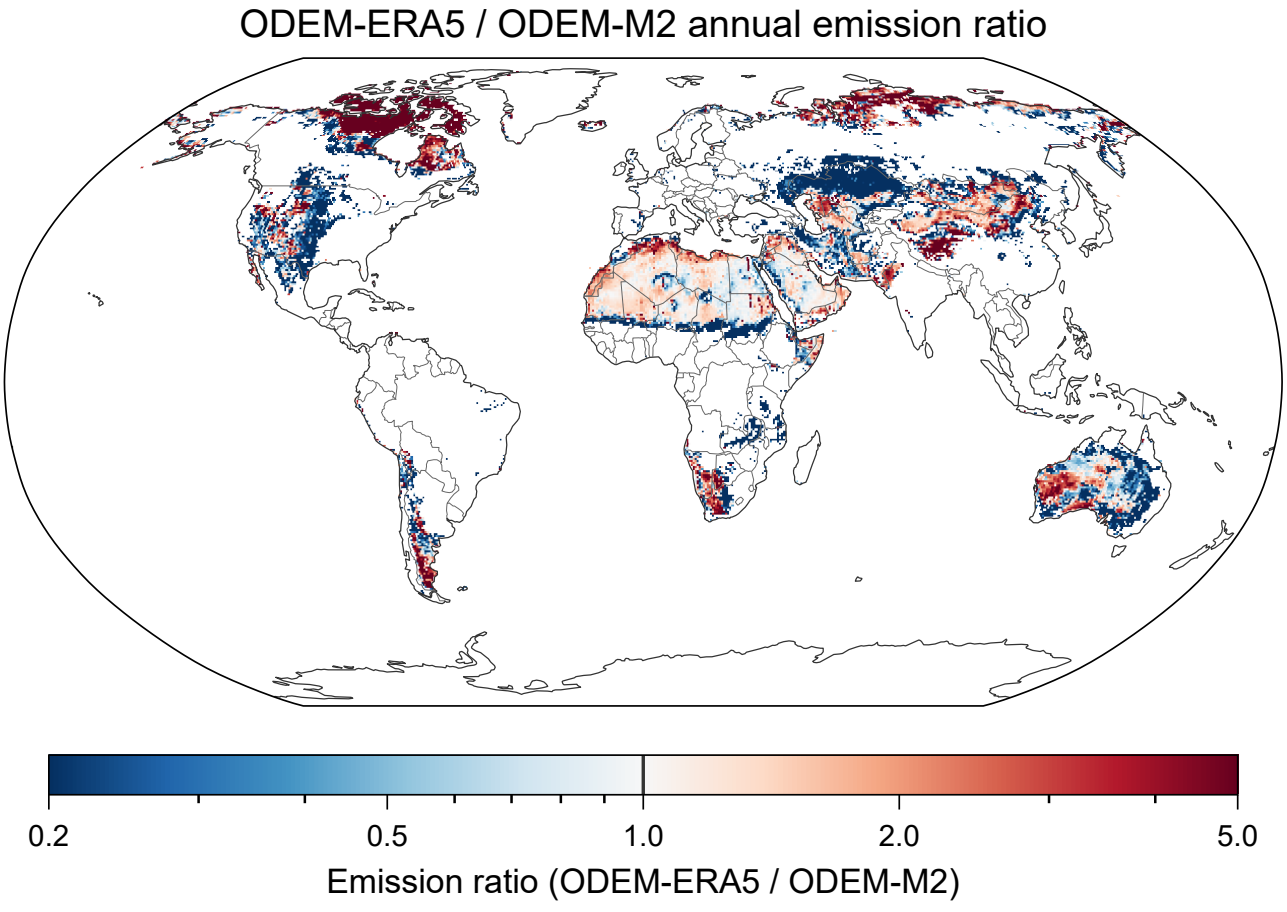

Figure 5. Grid-cell ratio of annual mean dust emission flux (ODEM-ERA5 / ODEM-M2, log scale) for 2006 after regridding ERA5 output to the MERRA-2 grid. Values above 1 (red) indicate higher ERA5 emission; values below 1 (blue) indicate higher MERRA-2 emission. Median ratio across active source cells is 0.99.

https://doi.org/10.5194/egusphere-2026-1905
Preprint. Discussion started: 11 May 2026

4.3 Regional budgets

Figure 6 compares regional emission budgets against the observational estimates of Kok et al. (2021). North Africa is the dominant source in all datasets, contributing 68 % (ODEM-ERA5) and 68 % (ODEM-M2) of global emission. Both ODEM experiments exceed the Kok et al. (2021) central estimate for North Africa (ERA5: 10 540; M2: 8720 vs. 6818 Tg yr^{-1}), though both remain within the large observational uncertainty range.

For the Middle East, both experiments exceed the Kok et al. (2021) central estimate (995 Tg yr^{-1}): ODEM-ERA5 yields 2580 Tg yr^{-1} and ODEM-M2 yields 2213 Tg yr^{-1}, both within the uncertainty bounds. In East Asia, ODEM-ERA5 (1485 Tg yr^{-1}) is close to the Kok et al. (2021) estimate (1250 Tg yr^{-1}), while ODEM-M2 (990 Tg yr^{-1}) is somewhat lower. This regional pattern — MERRA-2 producing relatively less emission in North Africa and East Asia compared to ERA5 — partially offsets the global difference and helps explain why the ODEM-M2 global total is closer to the observational constraint.

Australia (ODEM-ERA5: 319; ODEM-M2: 327 Tg yr^{-1}) compares well with Kok et al. (2021) (450 Tg yr^{-1}). The smaller source regions (North America, South America, southern Africa) are more uncertain observationally but are broadly captured by both experiments.

https://doi.org/10.5194/egusphere-2026-1905
Preprint. Discussion started: 11 May 2026

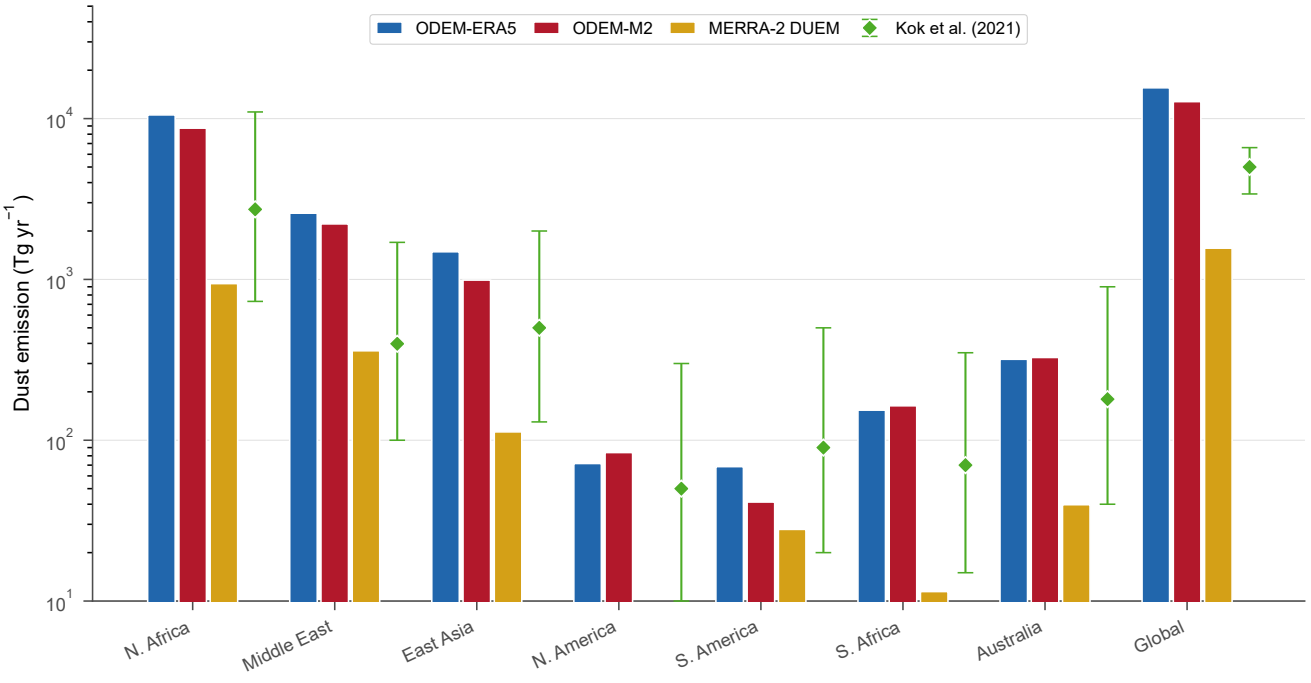

Figure 6. Regional dust emission budgets (Tg yr^{-1}, log scale) for 2006. Bars show ODEM-ERA5, ODEM-M2, and MERRA-2 DUEM. Green diamonds with error bars show the Kok et al. (2021) observational constraint (central estimate and range).

4.4 Seasonal cycle

Figure 7 shows the monthly global dust emission timeseries for 2006. Both ODEM experiments display a boreal spring–summer maximum (March–July) and a winter minimum, consistent with the known seasonality of dust emission driven by surface wind variability over the Northern Hemisphere source regions.

ODEM-ERA5 peaks in June at approximately 1500 Tg month^{-1}, while ODEM-M2 shows a broader peak from March to July, reaching approximately 1350 Tg month^{-1}. The ODEM-ERA5 curve lies consistently above ODEM-M2 throughout the year, with the largest absolute difference during the boreal summer. MERRA-2 DUEM shows a similar seasonal phase but at roughly one order of magnitude lower amplitude, consistent with the global budget difference.

The Kok et al. (2021) annual mean range (divided by 12 for monthly comparison) brackets the MERRA-2 DUEM values throughout the year. Both ODEM experiments exceed this range throughout the year at the default calibration ($C_{\text{tune}} = 0.05$); normalising to $C_{\text{tune}} = 0.020$ (Sect. 5.3) would scale the ODEM curves into the shaded band without altering their seasonal phasing.

The monthly timeseries also reveals the regional drivers of this seasonality. Over North Africa, emission peaks in boreal summer (JJA), driven by the intensification of the Saharan heat low and associated strengthening of surface winds. The Arabian Peninsula and Middle East follow a similar phase. East Asia shows a spring maximum (MAM), consistent with the known

https://doi.org/10.5194/egusphere-2026-1905
Preprint. Discussion started: 11 May 2026

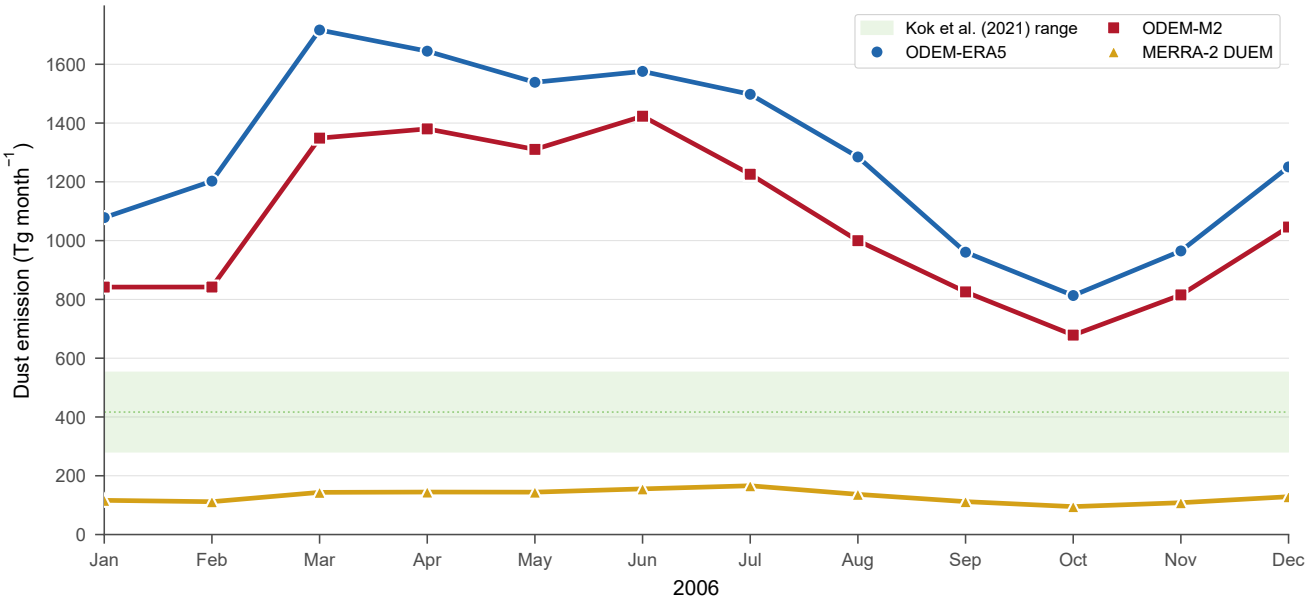

Figure 7. Monthly global dust emission totals (Tg month^{-1}) for 2006 at the default calibration ($C_{\text{tune}} = 0.05$). The green shaded band shows the Kok et al. (2021) PM20 annual mean range divided by 12 for reference. Normalising to $C_{\text{tune}} = 0.020$ (Sect. 5.3) scales all curves by 0.4 without changing their shape.

East Asian dust season. ODEM-ERA5 and ODEM-M2 agree on the seasonal phasing across all regions, with the amplitude differences between the two experiments consistent with the annual mean ratio.

4.5 Comparison with DustCOMM

Figure 8 compares ODEM emission with the observationally constrained DustCOMM dust loading climatology of Adebiyi et al. (2020). While emission flux and column loading are not directly equivalent — loading integrates transport and deposition — the spatial correlation between source regions and high-loading areas provides an independent check on whether ODEM places emission in the right locations.

Panel (c) shows the DustCOMM annual mean dust loading, and panels (a,b) show the corresponding ODEM-ERA5 and ODEM-M2 emission maps for comparison. The log-log scatter of ODEM-M2 emission against DustCOMM loading (panel d) yields $R = 0.72$. Because direct validation against surface emission observations is not possible at the global scale, this spatial comparison provides a qualitative check on whether ODEM places emission in source regions consistent with observed dust loading. High loading in the tropical North Atlantic and Arabian Sea, which reflect transport from the Sahara and Arabian sources respectively, correspond to the highest ODEM emission cells. However, this correlation conflates emission strength with atmospheric transport: high-loading regions include not only source areas but also their immediate downwind transport corridors (e.g., the tropical North Atlantic), so $R = 0.72$ reflects spatial co-location of sources and plumes rather than a di-

https://doi.org/10.5194/egusphere-2026-1905
Preprint. Discussion started: 11 May 2026

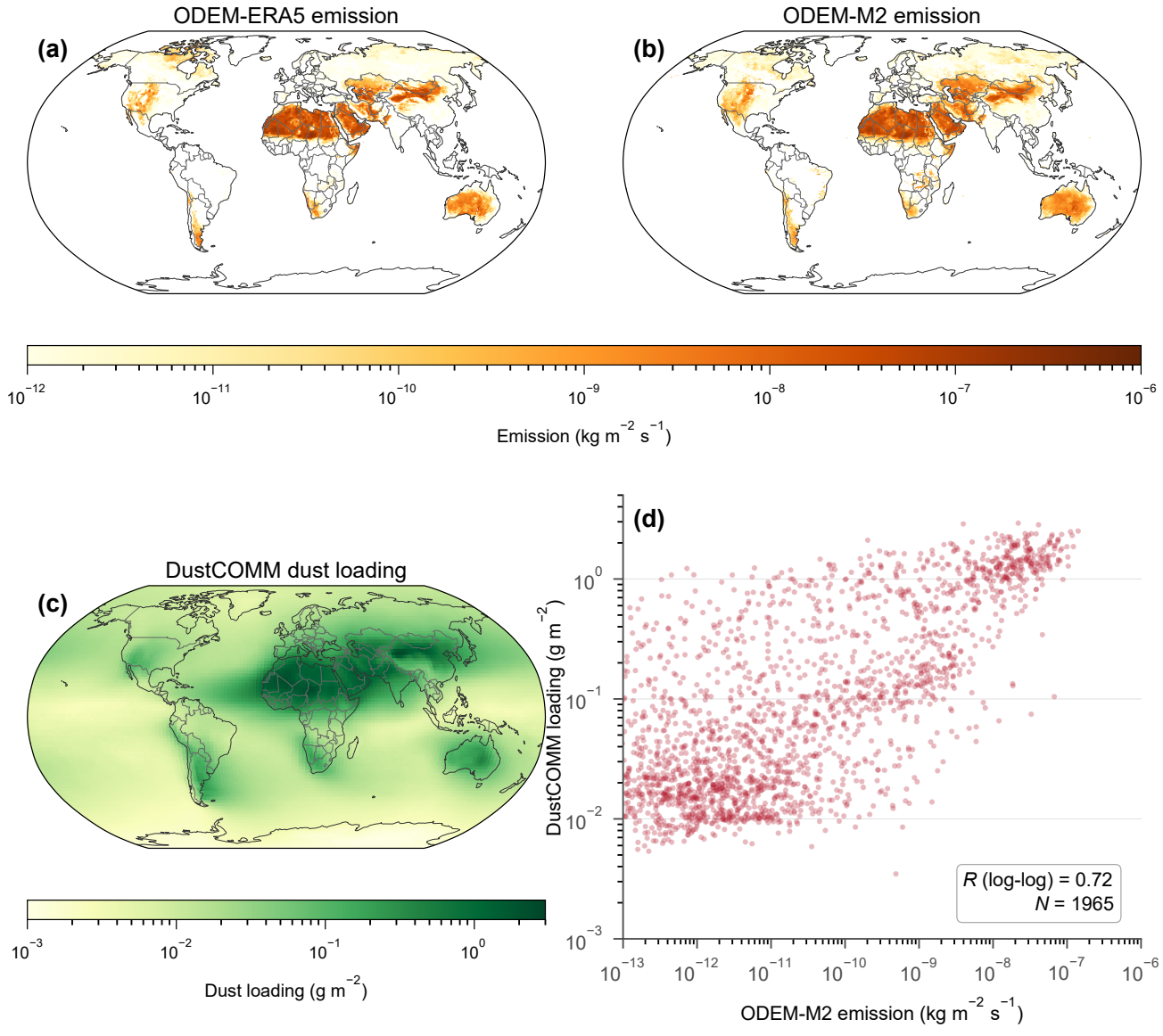

Figure 8. Comparison of ODEM emission with DustCOMM dust loading (Adebiyi et al., 2020). (a) ODEM-ERA5 annual emission, (b) ODEM-M2 annual emission (both $\mathrm{kg\,m^{-2}\,s^{-1}}$, log scale), (c) DustCOMM annual mean dust loading ($\mathrm{g\,m^{-2}}$, log scale), (d) log-log scatter of ODEM-M2 emission vs DustCOMM loading at matched grid cells ($R = 0.72$).

rect emission validation. Both fields are also dominated by the Saharan signal, which inflates the correlation through spatial autocorrelation; the value should not be interpreted as a quantitative validation metric.

https://doi.org/10.5194/egusphere-2026-1905
Preprint. Discussion started: 11 May 2026

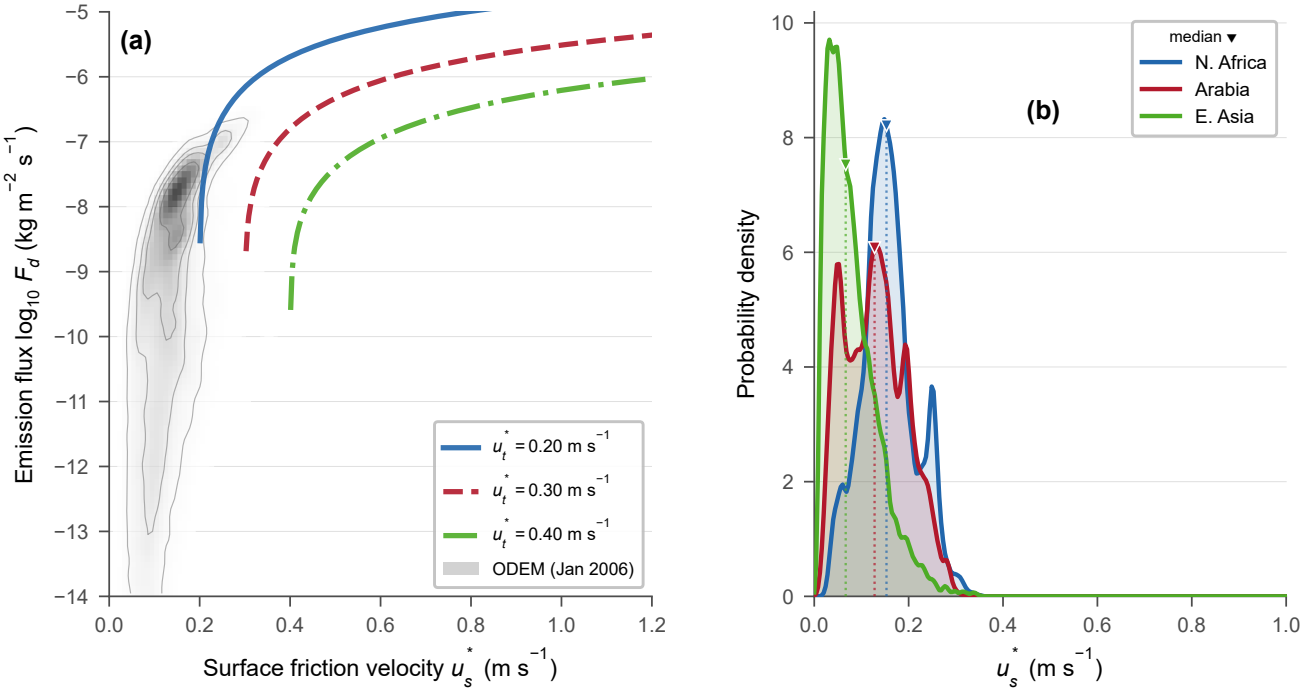

Figure 9. (a) Dust emission flux versus surface friction velocity. Coloured lines show the theoretical Kok (2011) emission curve for three threshold values; grey shading shows the density of ODEM grid-cell monthly mean values (January 2006). (b) Probability density of surface friction velocity u_{*s} at three major source regions. Downward triangles mark the median.

4.6 Emission physics verification

Figure 9 verifies that ODEM correctly implements the brittle fragmentation emission equation. Panel (a) shows the theoretical F_d–u_{*s} relationship (Eq. 9) for three threshold friction velocities, overlaid on the density of ODEM grid-cell emission values from January 2006. The simulated emission follows the theoretical curves closely, confirming that the numerical implementation reproduces the expected nonlinear scaling.

Panel (b) shows the probability density of surface friction velocity u_{*s} at three major source regions: North Africa, Arabia, and East Asia. North Africa has the highest median u_{*s}, consistent with its dominance of the global dust budget. Arabia shows a broader distribution extending to higher u_{*s} values, while East Asia has a narrower distribution centred at lower values, consistent with the relatively lower emission from this region.

https://doi.org/10.5194/egusphere-2026-1905
Preprint. Discussion started: 11 May 2026

5 Discussion

5.1 Sensitivity to meteorological forcing

ERA5 produces 22 % more global emission than MERRA-2, showing that reanalysis choice alone shifts the global dust budget by more than one fifth, even when the emission physics are held constant. The difference is spatially structured (Fig. 4): ERA5 produces stronger emission over the central and western Sahara, while MERRA-2 produces stronger emission over parts of the Arabian Peninsula and East Asia. This pattern is consistent with known differences in the surface friction velocity fields between the two reanalyses (Hersbach et al., 2020; Gelaro et al., 2017). The IFS model underlying ERA5 (Hersbach et al., 2020) and the GEOS-5 model underlying MERRA-2 (Molod et al., 2015) use different boundary layer and surface layer parameterisations, which produce systematically different u_* fields — particularly over arid surfaces where roughness lengths are small and the friction velocity is sensitive to the turbulence closure.

ODEM-M2 distributes emission more evenly across source regions — less concentrated in North Africa, more in the Middle East and East Asia — resulting in a regional budget that agrees better with the observational constraints of Kok et al. (2021). This suggests that the ERA5 friction velocity may be biased high over the Sahara relative to MERRA-2, or that MERRA-2 better captures the wind regime in secondary source regions.

Figure 10 characterises the u_* differences directly. Panel (a) shows a 2D density scatter of annual mean friction velocity at source grid cells, with ERA5 regridded to the MERRA-2 grid for comparison. Across all source cells, MERRA-2 u_* is on average higher than ERA5 ($R = 0.419$, mean bias $= -0.074\,\mathrm{m\,s^{-1}}$, computed as ERA5 minus MERRA-2). Panel (b) shows the zonal mean u_* profiles at source cells (clipped to $\pm 45°$ where most dust sources are active): MERRA-2 exceeds ERA5 at most latitudes, with ERA5 higher only in a narrow band near 0–10° N. Despite this, ERA5 produces 22 % more global emission because it generates higher u_* specifically over the central and western Sahara — the cells that contribute the largest absolute fluxes. Because the emission equation responds nonlinearly to u_* above threshold, these localised ERA5 excesses in the high-flux tail outweigh the broader MERRA-2 advantage at moderate u_* values.

https://doi.org/10.5194/egusphere-2026-1905
Preprint. Discussion started: 11 May 2026

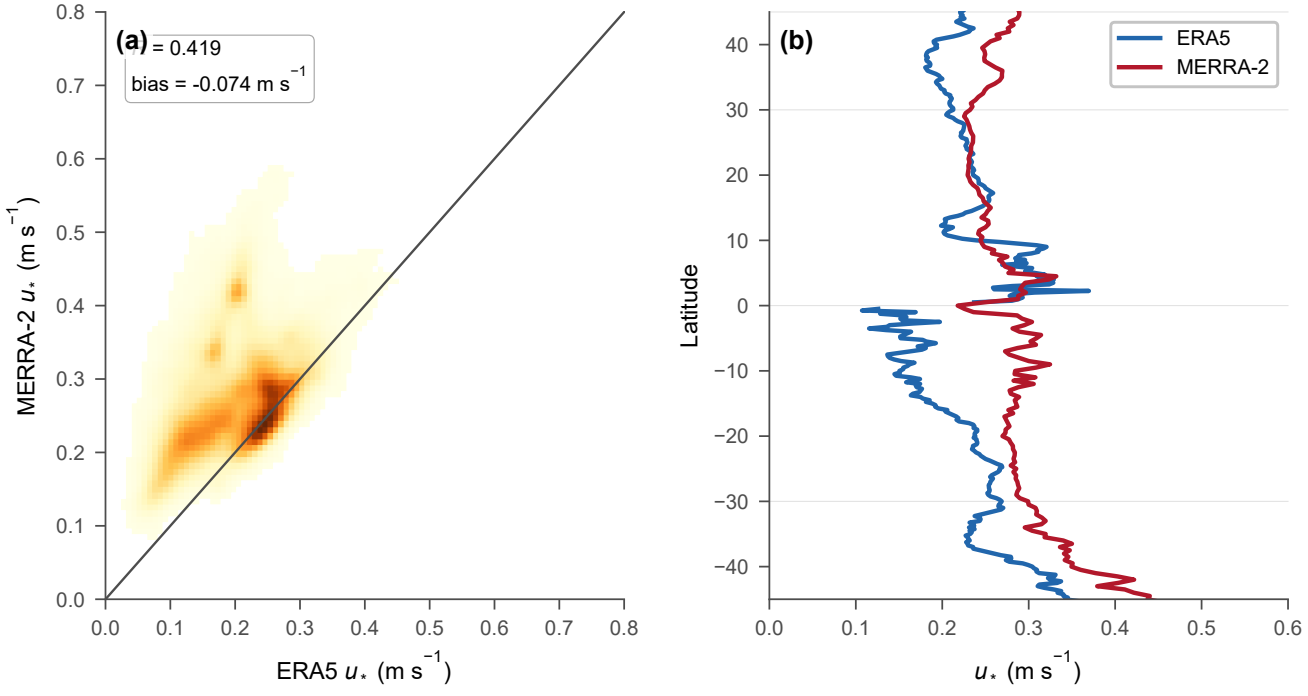

Figure 10. Comparison of annual mean friction velocity u_* between ERA5 and MERRA-2 at dust source grid cells (2006). (a) 2D density scatter of ERA5 vs MERRA-2 u_* after regridding ERA5 to the MERRA-2 grid; the 1:1 line is shown in grey. (b) Zonal mean u_* profiles at source cells for ERA5 (blue) and MERRA-2 (red), shown for $\pm 45^\circ$ latitude.

5.2 Effect of temporal resolution

Because dust emission is a threshold process, the temporal resolution of the forcing influences how much sub-timestep wind variability is captured. Coarser averaging smooths out short-lived high-wind events, potentially suppressing emission where the 3-hourly mean u_* falls below threshold even though instantaneous values would exceed it. ODEM compensates for this through the turbulent intermittency correction (Sect. 2.4.9), which estimates the fraction of each timestep during which saltation is active based on a Gaussian wind speed distribution.

To quantify this effect, ERA5 was additionally run at 1-hourly resolution (8760 timesteps per year; ODEM-ERA5 in Table 5) and at 3-hourly resolution (2920 timesteps per year; ODEM-ERA5 (3 h)). The 3-hourly forcing was obtained from the Copernicus Climate Data Store at 3-hourly time steps, not subsampled from the locally stored 1-hourly archive. The 1-hourly run produces 15 539 Tg yr^{-1} and the 3-hourly run produces 15 521 Tg yr^{-1}, a difference of 0.1 %. This negligible sensitivity confirms that the turbulent intermittency correction effectively accounts for sub-3-hourly wind variability and that the choice of ERA5 temporal resolution does not meaningfully bias the emission estimate. The 1-hourly result is adopted as the primary ODEM-ERA5 experiment because it uses the full resolution of the ERA5 archive.

https://doi.org/10.5194/egusphere-2026-1905
Preprint. Discussion started: 11 May 2026

Table 6. Effect of C_{tune} on global annual dust emission (Tg yr^{-1}). Because C_{tune} is a linear factor, all entries in the normalised column equal the default column $\times 0.4$, and all ratios are preserved exactly.

	$C_{\text{tune}} = 0.05$	$C_{\text{tune}} = 0.020$	Kok (2021)
ODEM-ERA5 (1 h)	15 539	6216	
ODEM-ERA5 (3 h)	15 521	6208	
ODEM-M2	12 747	5099	5000*
ERA5 / M2 ratio	1.22	1.22	
1 h / 3 h difference	0.1 %	0.1 %	

*PM20 central estimate (3400–6600) Tg yr^{-1}.

The 22 % difference between ODEM-ERA5 and ODEM-M2 therefore cannot be attributed to temporal resolution. It reflects differences in u_* magnitude and spatial distribution between the two reanalyses — primarily over the central Sahara, where ERA5 produces substantially stronger surface winds than MERRA-2 (Fig. 10). Nor can the difference be attributed to spatial interpolation: the global emission totals in Table 5 are computed at each reanalysis's native resolution. Regridding ERA5 to the coarser MERRA-2 grid for the cell-by-cell comparisons (Figs. 4, 5, 10) smooths the ERA5 field, which would suppress rather than amplify any ERA5 excess.

5.3 Sensitivity to the calibration constant

The global tuning constant C_{tune} enters the Kok et al. (2014) emission equation (Eq. 9) as a linear multiplicative factor. Changing C_{tune} therefore scales all emission fluxes proportionally without altering spatial patterns, temporal variability, or reanalysis ratios. Table 6 demonstrates this by comparing the default calibration ($C_{\text{tune}} = 0.05$, from Leung et al., 2023) with a normalised calibration ($C_{\text{tune}} = 0.020$) that brings ODEM-M2 into agreement with the Kok et al. (2021) PM20 central estimate of 5000 Tg yr^{-1}.

Under the normalised calibration, ODEM-M2 produces 5099 Tg yr^{-1}, within the $\pm 1\sigma$ observational range. The 22 % ERA5–MERRA-2 difference, the 0.1 % temporal resolution insensitivity, and all spatial correlation metrics are invariant to the choice of C_{tune}. The normalised outputs are provided in the data archive and can be independently reproduced by running ODEM with the `--C-tune 0.020` command-line flag.

5.4 Comparison with MERRA-2 online emission

The factor-of-ten difference between ODEM and MERRA-2 DUEM reflects fundamental differences in emission physics rather than forcing, since ODEM-M2 and DUEM use the same MERRA-2 meteorology. The GOCART scheme in MERRA-2 is an empirical parameterisation that scales emission linearly with a source function and a threshold-dependent wind term (Ginoux et al., 2001), whereas the Kok et al. (2014) scheme produces a steeper, nonlinear response through the fragmentation exponent.

https://doi.org/10.5194/egusphere-2026-1905
Preprint. Discussion started: 11 May 2026

The DUEM value of 1564 Tg yr^{-1} falls well below the Kok et al. (2021) observational range, confirming the known low bias of the GOCART scheme.

5.5 Limitations and outlook

ODEM v1.0 has several limitations.

First, the global tuning constant $C_{\text{tune}} = 0.05$ was inherited from Leung et al. (2023), who chose this value for the Kok et al. (2014) emission equation within CESM. Without post-hoc normalisation, both ODEM and the Leung et al. (2023) scheme overshoot the Kok et al. (2021) PM20 constraint by a factor of ∼2.5 (ODEM-M2: 12 747 vs. 5000 Tg yr^{-1}; Leung: ∼11 700 vs. 5000 Tg yr^{-1}). Leung et al. (2023) attribute this to the inability of current emission physics to constrain the absolute magnitude from first principles, and normalise their results to the PM20 constraint. As shown in Sect. 5.3, normalising to the PM20 central estimate ($C_{\text{tune}} = 0.020$) brings ODEM-M2 within the observational range while preserving all spatial patterns and reanalysis ratios exactly (Table 6). Part of this overshoot may reflect structural errors in the traditional drag partition rather than the emission physics itself. Chappell et al. (2023) showed that the Marticorena and Bergametti (1995) scheme uses a nearly constant sheltering ratio ($R \approx 0.91$) that inadequately represents the spatial variability of surface roughness, forcing C_{tune} to absorb the resulting bias. Replacing the traditional drag partition with a satellite-observed albedo-based sheltering approach (Chappell and Webb, 2016; LeGrand et al., 2023) reduces untuned emission by an order of magnitude relative to the default Kok et al. (2014) scheme, suggesting that a physically constrained drag partition could substantially reduce the need for global tuning. Implementing and evaluating this approach within ODEM is the subject of a follow-up study. More broadly, C_{tune} serves a role analogous to the mass-budget proportionality constant C_{MB} introduced by Zender et al. (2003), who used it to bridge the gap between local-scale saltation fluxes and grid-cell-mean dust emission — reflecting the physical reality that not all saltated particles produce vertical dust flux. Unlike C_{MB}, which was motivated by this scale-bridging argument, C_{tune} in the Kok et al. (2014) framework lacks an explicit physical derivation. A physically grounded version of this constant could depend on soil properties such as the clay-to-rock ratio or the particle size distribution of the parent material, which control what fraction of the saltation flux is converted to suspended dust. Developing such a parameterization would reduce the reliance on post-hoc tuning and is a priority for future ODEM versions.

Second, the erodibility mask is derived from a single year of MODIS land cover, which may not capture interannual land use changes. In particular, the Sahel boundary and agricultural expansion in semi-arid regions evolve on decadal timescales, and a static mask may introduce biases in multi-year simulations.

Third, ODEM does not account for supply limitation. In reality, dust emission can deplete the available loose sediment at the surface, particularly in low-supply regions. The current formulation assumes an unlimited reservoir of erodible material. Including a sediment availability term is a priority for ODEM v2.0.

Fourth, ODEM does not represent surface crusting, desert pavement formation, or the aerodynamic Owen effect, all of which can modify emission thresholds and fluxes at local scales.

https://doi.org/10.5194/egusphere-2026-1905
Preprint. Discussion started: 11 May 2026

Fifth, the model produces total dust emission without explicit size segregation. While the Kok (2011) size distribution is implicit in the emission coefficient C_d, resolving size-binned emission fluxes would be needed for coupling to aerosol transport models that track multiple size bins.

Sixth, only a single year (2006) was evaluated. Extending the analysis to a multi-year period would allow assessment of interannual variability and trend sensitivity, particularly in the context of observed changes in Saharan dust emission over recent decades.

6 Conclusions

This paper has presented ODEM v1.0, an offline dust emission model that applies the brittle fragmentation emission parameterization of Kok et al. (2014) to externally prescribed reanalysis forcing. The key findings are:

1. ODEM driven by MERRA-2 produces a global PM20 emission of 12 747 Tg yr^{-1} for 2006, exceeding the Kok et al. (2021) observationally constrained PM20 budget of 5000 ± 1600 Tg yr^{-1} by a factor of 2.5. This overshoot is consistent with the factor-of-2.3 reported by Leung et al. (2023) for the same emission equation and reflects the documented inability of current emission physics to constrain absolute emission magnitude from first principles. ODEM driven by ERA5 at 1-hourly resolution produces 15 539 Tg yr^{-1} (factor 3.1).

2. With identical emission physics, ERA5 produces 22 % more emission than MERRA-2 and concentrates it more strongly over the central Sahara, while MERRA-2 distributes emission more toward the Arabian Peninsula and East Asia. This demonstrates that the choice of reanalysis is a significant source of uncertainty in dust emission estimates.

3. A sensitivity experiment using ERA5 at 3-hourly resolution (15 521 Tg yr^{-1}) differs by only 0.1 % from the 1-hourly result, confirming that the turbulent intermittency correction effectively accounts for sub-timestep wind variability.

4. Both ODEM experiments produce roughly an order of magnitude higher emission than the MERRA-2 online GOCART scheme, consistent with the known underestimation by empirical parameterisations relative to observational constraints.

5. The offline approach separates forcing uncertainty from physics uncertainty, which is not possible in online models. ODEM can serve as an emission driver for Lagrangian transport models and as a testbed for evaluating emission scheme improvements.

ODEM v1.0 source code is freely available under the MIT licence. Future development will focus on sediment supply limitation, size-resolved emission, and multi-year climatological runs. Because ODEM accepts any reanalysis as input, running it with multiple products (e.g. ERA5, MERRA-2, JRA-3Q) produces an emission ensemble whose spread directly quantifies forcing uncertainty — an approach not possible with online models. Potential applications include dust source attribution during extreme transport events such as atmospheric rivers, dust-driven nutrient deposition budgets, solar energy yield loss estimation, and particulate number exposure assessments for health impact studies. A companion emission processing framework,

https://doi.org/10.5194/egusphere-2026-1905
Preprint. Discussion started: 11 May 2026

currently under development, combines ODEM output with source-receptor relationships from FLEXPART and HYSPLIT to compute trajectory-level dust emission and particulate number concentrations along transport pathways.

Code availability. ODEM v1.0 source code is archived on Zenodo (https://doi.org/10.5281/zenodo.19390605, Baykara, 2026a) and available at https://github.com/Metn/odem under the MIT licence.

Data availability. All input datasets used by ODEM v1.0 are freely available from the original providers. ERA5 reanalysis data (Hersbach et al., 2020) are available from the Copernicus Climate Data Store (https://cds.climate.copernicus.eu). MERRA-2 reanalysis data (Gelaro et al., 2017) are available from the NASA Goddard Earth Sciences Data and Information Services Center, GES DISC (https://disc.gsfc.nasa.gov). Static input datasets (also summarised in Table 1) are: SoilGrids v2.0 soil texture and bulk density (Poggio et al., 2021), available from https://soilgrids.org; MODIS MCD12C1 land cover (Friedl and Sulla-Menashe, 2015), available from https://lpdaac.usgs.gov/products/mcd12c1v006/; Copernicus Global Land Service bare soil cover fraction (Copernicus Global Land Service, 2020), available from https://land.copernicus.eu/global/products/lc; satellite-derived aerodynamic roughness length (Prigent et al., 2005); and MODIS MCD15A2H leaf area index (Myneni et al., 2015), available from https://lpdaac.usgs.gov/products/mcd15a2hv006/. Model output for the ERA5 and MERRA-2 experiments presented in this paper is archived on Zenodo (https://doi.org/10.5281/zenodo.19320862, Baykara, 2026b).

Author contributions. MB developed the model, performed all simulations, conducted the analysis, and wrote the manuscript.

Competing interests. The author declares no competing interests.

Acknowledgements. Generated using Copernicus Climate Change Service information 2024. Neither the European Commission nor ECMWF is responsible for any use that may be made of the Copernicus information or data it contains. MERRA-2 data were provided by the Global Modeling and Assimilation Office (GMAO) at NASA Goddard Space Flight Center through the NASA GES DISC. The authors wish to acknowledge CSC – IT Center for Science, Finland, for computational resources.

Financial support. This research received no external funding.

https://doi.org/10.5194/egusphere-2026-1905
Preprint. Discussion started: 11 May 2026

References

Adebiyi, A. A., Kok, J. F., Wang, Y., Ito, A., Ridley, D. A., Nabat, P., and Zhao, C.: Dust constraints from joint observational-modelling-experimental analysis – DustCOMM version 1, Atmos. Chem. Phys., 20, 829–863, https://doi.org/10.5194/acp-20-829-2020, 2020.

Baykara, M.: ODEM v1.0: an offline dust emission model (v1.0), https://doi.org/10.5281/zenodo.19390605, 2026a.

Baykara, M.: ODEM v1.0 model output: global dust emission fluxes for 2006 driven by ERA5 and MERRA-2, https://doi.org/10.5281/zenodo.19320862, 2026b.

Chappell, A. and Webb, N. P.: Using albedo to reform wind erosion modelling, mapping and monitoring, Aeolian Res., 23, 63–78, https://doi.org/10.1016/j.aeolia.2016.09.006, 2016.

Chappell, A., Webb, N. P., LeGrand, S. L., Ziegler, N. P., and Edwards, B. L.: Hidden weaknesses of dust emission modeling can be revealed by comparisons with AEM, J. Geophys. Res. Atmos., 128, e2023JD039 065, https://doi.org/10.1029/2023JD039065, 2023.

Comola, F., Kok, J. F., Chamecki, M., and Martin, R. L.: The intermittency of wind-driven sand transport, Geophys. Res. Lett., 46, 13 430–13 440, https://doi.org/10.1029/2019GL085739, 2019.

Copernicus Global Land Service: Fractional cover 300m, version 1, https://land.copernicus.eu/global/products/fc, accessed: 2026-03-20, 2020.

Fécan, F., Marticorena, B., and Bergametti, G.: Parametrization of the increase of the aeolian erosion threshold wind friction velocity due to soil moisture for arid and semi-arid areas, Ann. Geophys., 17, 149–157, https://doi.org/10.1007/s00585-999-0149-7, 1999.

Friedl, M. A. and Sulla-Menashe, D.: MCD12C1 MODIS/Terra+Aqua Land Cover Type Yearly L3 Global 0.05Deg CMG V006, NASA EOSDIS Land Processes DAAC, https://doi.org/10.5067/MODIS/MCD12C1.006, 2015.

Gelaro, R., McCarty, W., Suárez, M. J., Todling, R., Molod, A., Takacs, L., Randles, C. A., Darmenov, A., Bosilovich, M. G., Reichle, R., Wargan, K., Coy, L., Cullather, R., Draper, C., Akella, S., Buchard, V., Conaty, A., Silva, A. M., Gu, W., Kim, G.-K., Koster, R., Lucchesi, R., Merkova, D., Nielsen, J. E., Partyka, G., Pawson, S., Putman, W., Rienecker, M., Schubert, S. D., Sienkiewicz, M., and Zhao, B.: The Modern-Era Retrospective Analysis for Research and Applications, Version 2 (MERRA-2), J. Climate, 30, 5419–5454, https://doi.org/10.1175/JCLI-D-16-0758.1, 2017.

Ginoux, P., Chin, M., Tegen, I., Prospero, J. M., Holben, B., Dubovik, O., and Lin, S.-J.: Sources and distributions of dust aerosols simulated with the GOCART model, J. Geophys. Res., 106, 20 255–20 273, https://doi.org/10.1029/2000JD000053, 2001.

Hersbach, H., Bell, B., Berrisford, P., Hirahara, S., Horányi, A., Muñoz-Sabater, J., Nicolas, J., Peubey, C., Radu, R., Schepers, D., Simmons, A., Soci, C., Abdalla, S., Abellan, X., Balsamo, G., Bechtold, P., Biavati, G., Bidlot, J., Bonavita, M., Chiara, G., Dahlgren, P., Dee, D., Diamantakis, M., Dragani, R., Flemming, J., Forbes, R., Fuentes, M., Geer, A., Haimberger, L., Healy, S., Hogan, R. J., Hólm, E., Janisková, M., Keeley, S., Laloyaux, P., Lopez, P., Lupu, C., Radnoti, G., Rosnay, P., Rozum, I., Vamborg, F., Villaume, S., and Thépaut, J.-N.: The ERA5 global reanalysis, Q. J. Roy. Meteor. Soc., 146, 1999–2049, https://doi.org/10.1002/qj.3803, 2020.

Huneeus, N., Schulz, M., Balkanski, Y., Griesfeller, J., Prospero, J., Kinne, S., Bauer, S., Boucher, O., Chin, M., Dentener, F., Diehl, T., Easter, R., Fillmore, D., Ghan, S., Ginoux, P., Grini, A., Horowitz, L., Koch, D., Krol, M. C., Landing, W., Liu, X., Mahowald, N., Miller, R., Morcrette, J.-J., Myhre, G., Penner, J., Perlwitz, J., Stier, P., Takemura, T., and Zender, C. S.: Global dust model intercomparison in AeroCom phase I, Atmos. Chem. Phys., 11, 7781–7816, https://doi.org/10.5194/acp-11-7781-2011, 2011.

Kok, J. F.: A scaling theory for the size distribution of emitted dust aerosols suggests climate models underestimate the size of the global dust cycle, Proc. Natl. Acad. Sci. USA, 108, 1016–1021, https://doi.org/10.1073/pnas.1014798108, 2011.

https://doi.org/10.5194/egusphere-2026-1905
Preprint. Discussion started: 11 May 2026

Kok, J. F., Mahowald, N. M., Fratini, G., Gillies, J. A., Ishizuka, M., Leys, J. F., Mikami, M., Park, M.-S., Park, S.-U., Van Pelt, R. S., and Zobeck, T. M.: An improved dust emission model – Part 1: Model description and comparison against measurements, Atmos. Chem. Phys., 14, 13 023–13 041, https://doi.org/10.5194/acp-14-13023-2014, 2014.

Kok, J. F., Adebiyi, A. A., Albani, S., Balkanski, Y., Checa-Garcia, R., Chin, M., Colarco, P. R., Hamilton, D. S., Huang, Y., Ito, A., Klose, M., Li, L., Mahowald, N. M., Miller, R. L., Obiso, V., Pérez García-Pando, C., Rocha-Lima, A., and Wan, J. S.: Contribution of the world's main dust source regions to the global cycle of desert dust, Atmos. Chem. Phys., 21, 8169–8193, https://doi.org/10.5194/acp-21-8169-2021, 2021.

LeGrand, S. L., Polashenski, C., Letcher, T. W., Creighton, G. A., Peckham, S. E., and Cetola, J. D.: The AFWA dust emission scheme for the GOCART aerosol model in WRF-Chem v3.9.1.1, Geosci. Model Dev., 16, 2009–2038, https://doi.org/10.5194/gmd-16-2009-2023, 2023.

Leung, D. M., Kok, J. F., Li, L., Okin, G. S., Prigent, C., Klose, M., Pérez García-Pando, C., Menut, L., Mahowald, N. M., Lawrence, D. M., and Chamecki, M.: A new process-based and scale-aware desert dust emission scheme for global climate models – Part 1: Description and evaluation against inverse modeling emissions, Atmos. Chem. Phys., 23, 6487–6523, https://doi.org/10.5194/acp-23-6487-2023, 2023.

Mahowald, N. M., Muhs, D. R., Levis, S., Rasch, P. J., Yoshioka, M., Zender, C. S., and Luo, C.: Change in atmospheric mineral aerosols in response to climate: Last glacial period, preindustrial, modern, and doubled carbon dioxide climates, J. Geophys. Res., 111, D10 202, https://doi.org/10.1029/2005JD006653, 2006.

Marticorena, B. and Bergametti, G.: Modeling the atmospheric dust cycle: 1. Design of a soil-derived dust emission scheme, J. Geophys. Res., 100, 16 415–16 430, https://doi.org/10.1029/95JD00690, 1995.

Menut, L., Bessagnet, B., Khvorostyanov, D., Beekmann, M., Blond, N., Colette, A., Coll, I., Curci, G., Foret, G., Hodzic, A., Mailler, S., Meleux, F., Monge, J.-L., Pison, I., Siour, G., Turquety, S., Valari, M., Vautard, R., and Vivanco, M. G.: CHIMERE 2013: a model for regional atmospheric composition modelling, Geosci. Model Dev., 6, 981–1028, https://doi.org/10.5194/gmd-6-981-2013, 2013.

Molod, A., Takacs, L., Suarez, M., and Bacmeister, J.: Development of the GEOS-5 atmospheric general circulation model: evolution from MERRA to MERRA2, Geosci. Model Dev., 8, 1339–1356, https://doi.org/10.5194/gmd-8-1339-2015, 2015.

Myneni, R., Knyazikhin, Y., and Park, T.: MOD15A2H MODIS/Terra Leaf Area Index/FPAR 8-Day L4 Global 500m SIN Grid V006, NASA EOSDIS Land Processes DAAC, https://doi.org/10.5067/MODIS/MOD15A2H.006, 2015.

Nickovic, S., Kallos, G., Papadopoulos, A., and Kakaliagou, O.: A model for prediction of desert dust cycle in the atmosphere, J. Geophys. Res., 106, 18 113–18 129, https://doi.org/10.1029/2000JD900794, 2001.

Okin, G. S.: A new model of wind erosion in the presence of vegetation, J. Geophys. Res., 113, F02S10, https://doi.org/10.1029/2007JF000758, 2008.

Panofsky, H. A., Tennekes, H., Lenschow, D. H., and Wyngaard, J. C.: The characteristics of turbulent velocity components in the surface layer under convective conditions, Bound.-Layer Meteorol., 11, 355–361, https://doi.org/10.1007/BF02186086, 1977.

Pisso, I., Sollum, E., Grythe, H., Kristiansen, N. I., Cassiani, M., Eckhardt, S., Arnold, D., Morton, D., Thompson, R. L., Zwaaftink, C. D. G., Evangeliou, N., Sodemann, H., Haimberger, L., Henne, S., Brunner, D., Burkhart, J. F., Fouber, A., Brioude, J., and Stohl, A.: The Lagrangian particle dispersion model FLEXPART version 10.4, Geosci. Model Dev., 12, 4955–4997, https://doi.org/10.5194/gmd-12-4955-2019, 2019.

Poggio, L., de Sousa, L. M., Batjes, N. H., Heuvelink, G. B. M., Kempen, B., Ribeiro, E., and Rossiter, D.: SoilGrids 2.0: producing soil information for the globe with quantified spatial uncertainty, SOIL, 7, 217–240, https://doi.org/10.5194/soil-7-217-2021, 2021.

https://doi.org/10.5194/egusphere-2026-1905
Preprint. Discussion started: 11 May 2026

Prigent, C., Tegen, I., Aires, F., Marticorena, B., and Zribi, M.: Estimation of the aerodynamic roughness length in arid and semi-arid regions over the globe with the ERS scatterometer, J. Geophys. Res., 110, D09 205, https://doi.org/10.1029/2004JD005370, 2005.

Randles, C. A., Silva, A. M., Buchard, V., Colarco, P. R., Darmenov, A., Govindaraju, R., Smirnov, A., Holben, B., Ferrare, R., Hair, J., Shinozuka, Y., and Flynn, C. J.: The MERRA-2 aerosol reanalysis, 1980 onward. Part I: System description and data assimilation evaluation, J. Climate, 30, 6823–6850, https://doi.org/10.1175/JCLI-D-16-0609.1, 2017.

Shao, Y.: Simplification of a dust emission scheme and comparison with data, J. Geophys. Res., 109, D10 202, https://doi.org/10.1029/2003JD004372, 2004.

Shao, Y. and Lu, H.: A simple expression for wind erosion threshold friction velocity, J. Geophys. Res., 105, 22 437–22 443, https://doi.org/10.1029/2000JD900304, 2000.

Stein, A. F., Draxler, R. R., Rolph, G. D., Stunder, B. J. B., Cohen, M. D., and Ngan, F.: NOAA's HYSPLIT atmospheric transport and dispersion modeling system, Bull. Am. Meteorol. Soc., 96, 2059–2077, https://doi.org/10.1175/BAMS-D-14-00110.1, 2015.

Tegen, I. and Fung, I.: Modeling of mineral dust in the atmosphere: Sources, transport, and optical thickness, J. Geophys. Res., 99, 22 897–22 914, https://doi.org/10.1029/94JD01928, 1994.

Zender, C. S., Bian, H., and Newman, D.: Mineral Dust Entrainment and Deposition (DEAD) model: Description and 1990s dust climatology, J. Geophys. Res., 108, 4416, https://doi.org/10.1029/2002JD002775, 2003.